https://doi.org/10.5194/wes-2026-142
Preprint. Discussion started: 18 August 2026

eawe european academy of wind energy
Open Access WIND ENERGY SCIENCE DISCUSSIONS

Static Closed-Loop Wake Steering and Induction Control in Floating Wind Farms for Load-Constrained Power Optimization

Federico Bellini[1,★], Majid Ebrahimi[1,★], Alessandro Fontanella[1], Sara Muggiasca[1], and Marco Belloli[1]
[1]Department of Mechanical Engineering, Politecnico di Milano, via La Masa 1, 20156 Milano, Italy
★These authors contributed equally to this work.
Correspondence: Majid Ebrahimi (majid.ebrahimi@polimi.it)

Abstract. This work develops and assesses static, closed-loop wind-farm flow-control strategies for load-constrained power optimization in a floating wind farm. Three farm-level strategies are considered: wake steering using turbine-specific nacelle-heading offsets, pitch-based induction control using discrete derating levels, and a hybrid yaw–induction strategy. A supervisory FLORIS engineering wake model computes the control setpoints by maximizing the predicted farm power. For induction and hybrid control, the power optimization is subject to a farm-level rotor-thrust constraint, which is used as an aerodynamic load-related proxy. The optimized setpoints are applied to a coupled FAST.Farm aero-hydro-servo-elastic model through independent ROSCO turbine controllers and a ZeroMQ communication interface. The resulting farm power, rotor thrust, structural loads, mooring loads, and spectral responses are then evaluated from the FAST.Farm simulations.

The investigated farm consists of four IEA 15 MW reference wind turbines mounted on UMaine VolturnUS-S semi-submersible platforms. The strategies are tested under below-rated turbulent wind conditions and compared against greedy operation, in which each turbine independently follows its maximum-power-point control strategy. The FLORIS model is calibrated against FAST.Farm response data using turbine power and thrust lookup tables for the considered derating levels together with wake-model parameter tuning.

The results show that all three strategies increase mean farm power relative to greedy operation, but with distinct power–load trade-offs. Within the investigated simulation matrix, hybrid control provides FAST.Farm-predicted farm-power gains ranging from 8.7% to 19%. Wake steering generally increases yaw-bearing damage-equivalent loads, whereas induction and hybrid control reduce yaw-bearing DELs and, to a lesser extent, blade-root moment DELs for most investigated conditions. Tower-base moment and fairlead-tension responses are less systematic and depend strongly on wind direction and coupled floating-platform–mooring dynamics. For the representative $U = 9\,\mathrm{m\,s^{-1}}$, $WD = -5°$ condition, spectral analysis shows that the controller-induced changes are concentrated in the rotor-harmonic and structural-frequency ranges and in the low-frequency platform–mooring region. Overall, the results demonstrate that load-constrained farm-power optimization can provide substantial power gains in floating wind farms, but that an aggregate rotor-thrust constraint alone does not prevent operating-condition-dependent structural and mooring-load penalties.

https://doi.org/10.5194/wes-2026-142
Preprint. Discussion started: 18 August 2026

WIND ENERGY SCIENCE DISCUSSIONS

1 Introduction

Floating offshore wind energy is increasingly important for expanding wind-power deployment into deep-water regions, where bottom-fixed foundations become technically or economically unfeasible. Floating wind turbines enable access to stronger and more persistent offshore wind resources, but they also introduce additional dynamic coupling between the rotor, floating platform response, mooring system dynamics, and incoming waves (Ji et al., 2024). These coupled aero-hydro-servo-elastic effects make the control problem more complex than for fixed-bottom wind turbines, particularly when multiple floating turbines operate in a wind farm (Ali et al., 2025; Carmo et al., 2024).

A major challenge in wind-farm operation is the interaction between downstream turbines and the wakes of upstream turbines. Upstream turbines extract energy from the incoming flow and generate velocity deficits and turbulence that propagate downstream. These wake effects reduce the power production of downstream turbines and can increase unsteady loading and fatigue damage (Chanprasert et al., 2022; Meyers et al., 2022). Consequently, greedy turbine-level operation, in which each turbine maximizes its own power output, is generally not optimal from the farm-level perspective. Farm-level control therefore aims to coordinate turbine operation and improve the overall power–load performance of the wind farm (Howland et al., 2019; Meyers et al., 2022).

Two widely investigated wind-farm control strategies are wake steering and static-axial-induction-based control. Wake steering intentionally yaw-misaligns selected turbines to redirect their wakes away from downstream machines. Although misalignment can reduce the power of the turbine that is yawed to achieve it, this strategy can increase total farm power by improving the inflow conditions of downstream turbines (Fleming et al., 2017, 2019; Doekemeijer et al., 2021). In contrast, static-axial-induction or derating control modifies the thrust and power extraction of selected turbines, for example through generator torque or blade-pitch adjustments, to reduce wake deficit and improve wake recovery (Boersma et al., 2017; Meyers et al., 2022). The performance of these strategies depends strongly on the wind-farm layout, inflow condition, accuracy of the wind farm simulator used for their assessment, and the selected control objectives (Meyers et al., 2022).

Many wind-farm control studies use open-loop strategies based on precomputed lookup tables obtained from steady-state engineering wake models. These approaches are attractive because they can provide setpoints with low computational cost, and they have demonstrated power gains in simulations and field experiments (Doekemeijer et al., 2021). However, open-loop control can be sensitive to the uncertainty of the model and the environmental conditions. Closed-loop control approaches address these limitations by using farm measurements or updated estimates of the inflow and farm state to recompute the control setpoints (Campagnolo et al., 2016; Doekemeijer et al., 2020; Becker et al., 2025).

Engineering wake models such as FLORIS are particularly suitable for online wind-farm control because they are computationally efficient and can evaluate many candidate control configurations during each optimization step (Fleming et al., 2023, 2020). However, these models are based on simplified wake formulations that depend on several user-defined or empirically determined parameters (King et al., 2021; van Binsbergen et al., 2024). When such a model is used to compute setpoints for a higher-fidelity dynamic plant or a real wind farm, model–plant mismatch can directly affect the selected control ac-

https://doi.org/10.5194/wes-2026-142
Preprint. Discussion started: 18 August 2026

tions and its effectiveness. Therefore, calibration of the wake model against representative simulation or operational data is an important step before using the engineering model for control-setpoint optimization (van Binsbergen et al., 2024).

These challenges are particularly relevant for floating wind farms. Floating-platform motions modify the relative inflow experienced by the rotor and interact with wake development and the response of downstream turbines (Johlas et al., 2019; Carmo et al., 2024). Hydrodynamic forcing and mooring-system dynamics also introduce load components and fluid–structure interactions that are absent or less prominent in bottom-fixed wind farms. Moreover, platform offsets governed by the mooring system can alter turbine positions, wake overlap, and the effectiveness of wake-steering control (Lozon et al., 2024). Although wind-farm control has been extensively investigated for land-based and fixed-bottom offshore farms, few studies have jointly evaluated wake steering, induction control, and hybrid yaw–induction control for floating wind farms using a coupled aero-hydro-servo-elastic plant model. Previous studies have examined floating-turbine wake interactions and wake-steering-induced load redistribution separately (Carmo et al., 2024; Thedin et al., 2024), but there remains a need to investigate farm-power optimization under aerodynamic load-related constraints while also assessing the fatigue loads, spectral load content, and the resulting power–load trade-offs.

This paper addresses this gap through a closed-loop floating wind-farm control framework that couples a calibrated FLORIS online optimizer with FAST.Farm simulations (Jonkman and Shaler, 2021) of a four-turbine floating wind farm. FAST.Farm simulates the dynamic aero-hydro-servo-elastic plant response, while the Reference Open-Source Controller (ROSCO) applies the turbine-level control commands (Abbas et al., 2022). A ZeroMQ interface enables online communication between the turbine controllers and the farm-level optimizer (NREL ROSCO Developers, 2026). The wake-steering controller maximizes the farm power predicted by FLORIS by selecting turbine-specific nacelle-heading offsets. The induction-control stage selects discrete blade-pitch-based derating setpoints by maximizing the FLORIS-predicted farm power subject to a farm-level rotor-thrust constraint. For induction control, this constraint is imposed relative to the non-derated, zero-yaw FLORIS baseline. In the hybrid strategy, wake steering is optimized first, after which the derating optimization is performed using the optimized yaw angles. The hybrid thrust constraint is therefore imposed relative to the corresponding non-derated, yawed FLORIS condition. The optimized yaw and derating setpoints are subsequently applied to FAST.Farm, while power, rotor thrust, structural loads, mooring loads, and spectral responses are evaluated a posteriori from the dynamic simulation results.

The main contribution of this work is the development and assessment of static, closed-loop wind-farm flow-control strategies for load-constrained power optimization in a floating wind farm. Specifically, the contributions are: (i) the formulation and implementation of wake steering, pitch-based induction control, and hybrid yaw–induction control in a floating wind-farm setting; (ii) the integration of these strategies within a closed-loop FLORIS–ROSCO–FAST.Farm framework that enables online setpoint updates and coupled aero-hydro-servo-elastic response evaluation; (iii) the calibration of the FLORIS engineering wake model against FAST.Farm response data using the considered floating-farm layout and derating-dependent turbine lookup tables; and (iv) the comparative assessment of load-constrained farm-power optimization using farm power, rotor thrust, fatigue damage-equivalent loads, load spectra, and combined power–load metrics.

The remainder of the paper is organized as follows. Section 2.1 introduces the reference floating wind farm, the FAST.Farm modeling approach, and the environmental conditions for the controller's evaluation. Section 2.5 describes the investigated

https://doi.org/10.5194/wes-2026-142
Preprint. Discussion started: 18 August 2026

closed-loop wind-farm control strategies, their implementation in the simulation framework, and the calibration of the FLORIS model against data from the FAST.Farm model, representing the "true" wind farm. Section 3 presents the power, fatigue-load, and power- and load-spectral results. Section 4 discusses the physical interpretation of the results, with particular attention to the large induction and hybrid power gains, the dependence of these gains on FAST.Farm wake representation under derated and combined yaw–induction operation, and the selected layout and simulation matrix. Finally, Section 5 summarizes the main findings and outlines future research directions.

2 Methodology

This section describes the floating wind-farm system considered in the study, the FAST.Farm simulation setup, the closed-loop control framework, and the post-processing methods used to assess power production and the fatigue loads.

2.1 Reference system and modelling tools

This section defines the floating wind-farm model and the numerical setup used for the FAST.Farm simulations.

2.1.1 Reference floating wind turbine

The wind farm considered in this study consists of four IEA 15 MW reference wind turbines mounted on UMaine VolturnUS-S semi-submersible platforms. The IEA 15 MW reference wind turbine is a three-bladed, upwind, variable-speed turbine with a rotor diameter of 240 m and a hub height of 150 m (Gaertner et al., 2020). The present study focuses on the below-rated operating region, where wake interactions have the strongest impact on farm performance. In this regime, turbine power and thrust are sensitive to changes in inflow velocity, yaw misalignment, and derating setpoints. Wake-induced velocity deficits therefore cause substantial power losses at downstream turbines, and farm-level control can effectively redistribute power extraction among turbines without the rated-power saturation that limits controllability above the rated wind speed.

The turbine is installed on the UMaine VolturnUS-S semi-submersible platform, which consists of one central column, three outer columns, and three catenary mooring lines (Allen et al., 2020). The main turbine and platform properties are summarized in Tables 1 and 2.

2.1.2 Floating wind-farm layout

The four turbines are arranged in a near-inline configuration with a streamwise spacing of $5D$, where D is the rotor diameter. A small lateral offset is introduced between consecutive turbines to promote partial wake overlap across the investigated wind directions. This layout choice is motivated by the primary objective of the study, namely assessing power gains and structural response under farm-level control of floating turbines. A fully aligned configuration was avoided because it can induce sustained yaw-direction oscillations in the nacelle, as reported by Baricchio et al. (2025). The three relative wind-direction cases considered in the study are generated in FAST.Farm simulations by rotating the complete farm configuration with respect to the fixed inflow direction. For each case, both the turbine coordinates and the corresponding mooring-line

https://doi.org/10.5194/wes-2026-142
Preprint. Discussion started: 18 August 2026

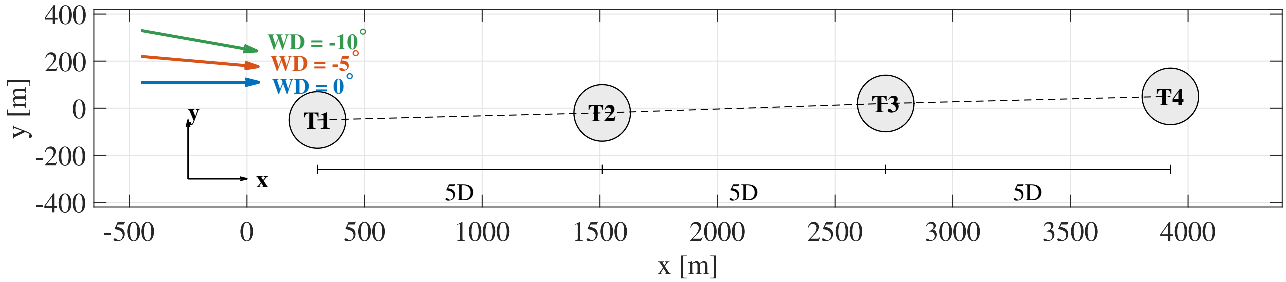

Figure 1. Floating wind-farm layout and inflow directions. Top-view schematic of the four-turbine floating wind-farm layout and the three inflow directions considered in this study. Turbines T1–T4 are arranged in a near-inline configuration with a small lateral offset and a streamwise spacing of $5D$. The arrows indicate the incoming wind directions $0°$, $-5°$, and $-10°$ relative to the nominal farm alignment.

layouts are rotated by the same angle, so that the relative orientation between each turbine, its floating platform, and its mooring system is preserved. Figure 1 illustrates the resulting farm orientations corresponding to relative wind directions of $0°$, $-5°$, and $-10°$.

2.2 FAST.Farm dynamic simulation model

The aero-hydro-servo-elastic response of the wind farm is simulated using FAST.Farm, which extends OpenFAST to multi-turbine arrays through a Dynamic Wake Meandering (DWM) framework (Jonkman and Shaler, 2021). FAST.Farm is a mid-fidelity dynamic wind farm model validated in previous studies against full-scale SCADA measurements (Shaler et al., 2020), high-fidelity large-eddy simulation (Jonkman et al., 2018; Rivera-Arreba et al., 2024) and controlled wind-tunnel measurements of turbine aerodynamic loads (Fontanella et al., 2025). In this framework, individual OpenFAST turbine models are coupled through the FAST.Farm inflow model, which represents atmospheric wind field, farm-level wake deficits, advection, meandering, deflection, and merging, while OpenFAST resolves the resulting aero-hydro-servo-elastic response and wake-induced loading of each turbine.

Table 1. Key parameters of the IEA 15 MW reference wind turbine (Gaertner et al., 2020).

Parameter	Value
Rotor orientation	Upwind, 3 blades
Cut-in, rated, cut-out wind speed	3 m/s, 10.59 m/s, 25 m/s
Minimum and maximum rotor speed	5.0 rpm, 7.56 rpm
Rotor diameter	240 m
Hub height	150 m
Drivetrain	Low-speed direct drive
Shaft tilt angle	6°

https://doi.org/10.5194/wes-2026-142
Preprint. Discussion started: 18 August 2026

The DWM model separates the turbulent inflow into large-scale and small-scale contributions. Large-scale turbulent structures govern wake advection and meandering, whereas smaller turbulent scales mainly contribute to wake recovery and turbulence mixing. To capture the large-scale velocity fluctuations responsible for wake meandering, the incoming turbulent wind field is low-pass filtered (Branlard et al., 2023). In the present study, the curl-wake formulation is used to represent wake deficits in all simulations because yaw misalignment and floating-platform motion can generate asymmetric wake structures. This makes the curl-wake representation more suitable than an axisymmetric wake model for the floating wind-farm control problem considered in Martínez-Tossas et al. (2021); Carmo et al. (2024); Jonkman and Shaler (2021).

Hydrodynamic loading on the floating substructure is computed using HydroDyn within the OpenFAST modelling framework. For the VolturnUS-S platform considered here, the hydrodynamic model is based on potential-flow theory using precomputed WAMIT coefficients, including hydrostatic restoring, added-mass and radiation effects, and wave-excitation loads. Viscous effects are represented through an additional global quadratic damping matrix rather than explicit Morison strip-theory members. Each floating wind turbine is therefore simulated with coupled aerodynamic, hydrodynamic, structural, mooring, and turbine-control dynamics.

FAST.Farm represents the wind field using separate low- and high-resolution domains in order to resolve farm-scale wake evolution and turbine-scale inflow without applying the finest spatial resolution over the entire computational domain. The low-resolution domain spans the full wind farm and is used to propagate ambient flow structures and wake meandering, while each turbine is embedded in a local high-resolution domain that resolves the rotor-scale inflow passed to OpenFAST.

The main FAST.Farm numerical settings are summarized in Table 3. FAST.Farm employs a two-level spatial discretisation. The low-resolution domain covers the entire farm and resolves the large-scale ambient flow and wake meandering dynamics, whereas individual high-resolution domains surround each rotor to provide the turbulent inflow required by the OpenFAST aero-elastic solver. The high-resolution time step is fixed at 0.1 s, while the low-resolution time step and streamwise spacing are adjusted according to the wind-speed condition.

Each simulation is run for 4600 s, and the initial transient is removed before computing the metrics of interest.

Table 2. Key parameters of the UMaine VolturnUS-S semi-submersible platform (Allen et al., 2020).

Parameter	Value
Hull displacement	20,206 m^3
Hull steel mass	3,914 t
Ballast mass, fixed/fluid	2,540/11,300 t
Draft	20 m
Vertical center of gravity from SWL	-14.94 m
Vertical center of buoyancy from SWL	-13.63 m
Roll/pitch inertia about center of gravity	1.251×10^{10} kg m^2
Yaw inertia about center of gravity	2.367×10^{10} kg m^2

https://doi.org/10.5194/wes-2026-142
Preprint. Discussion started: 18 August 2026

Table 3. Main FAST.Farm numerical settings used for the floating wind-farm simulations.

Parameter	**Value**
Ambient wind model, $Mod\_AmbWind$	3
Wake model, Mod_Wake	2, curl-wake formulation
Low-resolution domain size	$25D \times 5D \times 2.5D$
High-resolution domain size per turbine	$1.25D \times 1.25D$
Radial wake-grid spacing, dr	16 m
Number of radial wake nodes, NumRadii	24
Wake-advection cutoff frequency, f_c	0.008 Hz
Wake-meandering coefficient, C_{Meander}	2.1
Curl eddy-viscosity scaling, $k_{v,\mathrm{Curl}}$	5
High-resolution time step, DT_{High}	0.1 s
Low-resolution time step, DT_{Low}	0.8, 1 s
High-resolution grid spacing, dS_{High}	5 m
Low-resolution lateral/vertical spacing, dS_{Low}	15 m

2.3 Turbulent inflow and wave conditions

The simulations consider three below-rated mean hub-height wind speeds, $U_{\mathrm{hub}} \in \{7,8,9\}\ \mathrm{m\,s^{-1}}$, and three relative Wind Directions, $WD \in \{0°, -5°, -10°\}$. For each wind speed, five statistically independent turbulent wind realizations were generated, resulting in 15 unique wind fields. The same wind realizations were reused for the three wind-direction cases, which were represented by rotating the complete turbine and mooring-line configuration relative to the fixed inflow. This produced $3 \times 3 \times 5 = 45$ wind-condition cases.

The ambient wind fields were generated using TurbSim with the IEC Kaimal turbulence model. TurbSim generates time series of the three-component wind velocity over a spatial grid compatible with the FAST.Farm low- and high-resolution wind-domain requirements (Jonkman et al., 2014; OpenFAST Development Team, 2026). A turbulence intensity of 6% was prescribed at hub height, together with a power-law vertical shear profile of exponent equal to 0.06 (Türk and Emeis, 2010; Jeans, 2023) .

The wave condition was kept fixed for all the simulations, with a significant wave height of $H_s = 1$ m and a peak period of $T_p = 8$ s, consistent with the lower bound of the environmental range used by Sharma and Nava (2024) for floating-wind mooring-system simulations. Consequently, differences among the simulated cases arise from wind speed, relative wind direction, turbulent realization, and control strategy, rather than from variations in wave forcing.

2.4 Fatigue load calculation

Fatigue loading is assessed using short-term damage-equivalent loads (DELs) computed from the simulated load time series. The DELs are evaluated with MLife using rainflow counting, Goodman mean-load correction, and a fixed-mean formulation.

https://doi.org/10.5194/wes-2026-142
Preprint. Discussion started: 18 August 2026

The reported DELs correspond to one-sided amplitudes at an equivalent frequency of 1 Hz. For the blade-root, tower-base, and yaw-bearing bending moments, load roses are used and the maximum DEL over the considered directions is reported. The full fatigue post-processing procedure, including the Goodman correction, equivalent-cycle definition, ultimate-load assumptions, Wöhler exponents, and fatigue-channel definitions, is provided in Appendix A.

2.5 Control methodology

This section describes the closed-loop real-time control framework. FAST.Farm represents the dynamic floating wind-farm plant, ROSCO provides local turbine control, and FLORIS acts as the internal model for farm-level setpoint optimization. In addition to greedy operation, wake steering, induction control, and hybrid yaw–induction control are considered as shown in the workflow in Figure 2. Unlike a control implementation based exclusively on precomputed lookup tables, the present closed-loop supervisory controller updates the yaw and derating setpoints online using the current farm operating state. This allows the controller to adapt to changes in inflow conditions, wake interactions, and turbine availability that may differ from the conditions assumed during offline optimization. Such adaptability is particularly relevant for floating wind farms, where platform motions and wake–structure interactions introduce additional variability. Previous studies have shown that closed-loop estimation and online setpoint optimization can improve robustness and farm-level performance under time-varying inflow and plant changes compared with fixed open-loop policies (Doekemeijer et al., 2020; Bellini et al., 2026).

2.5.1 Closed-loop controller implementation

Each turbine is controlled by an independent ROSCO instance through the Bladed-style `DISCON` interface (Abbas et al., 2022).

Farm-level coordination of turbines is enabled through the ROSCO ZeroMQ wind-farm-control interface, with the external farm controller acting as the server and the turbine-side ROSCO instances acting as clients (NREL ROSCO Developers, 2026). At each communication step, ROSCO transmits turbine-level measurements, including turbine index within the farm, simulation time, power, rotational speeds, torque, nacelle orientation, blade-root bending moments, and rotor azimuth. The farm-level controller decodes these signals, estimates the operating condition, and computes updated turbine-specific setpoints using FLORIS.

For wake steering, the external wind-farm controller returns nacelle-heading offsets. For induction control, it returns pitch-related offsets associated with the selected derating levels. The hybrid strategy returns both yaw and pitch commands. These setpoints are transmitted back to the turbine-level ROSCO controllers through ZeroMQ and are applied locally by each turbine controller.

The closed-loop architecture is summarized in Figure 2. FAST.Farm provides the dynamic plant response, including wake evolution, platform motion, and coupled aero-hydro-servo-elastic turbine dynamics. The ROSCO controllers act as local turbine controllers and exchange turbine-level measurements and farm-level setpoints with the external FLORIS-based wind-farm controller. Within the external controller, the incoming measurements are filtered and used to update the estimated operating condition before computing the control commands. The wind-speed-estimation procedure is described separately in 2.5.3.

https://doi.org/10.5194/wes-2026-142
Preprint. Discussion started: 18 August 2026

eawe european academy of wind energy
Open Access WIND ENERGY SCIENCE DISCUSSIONS

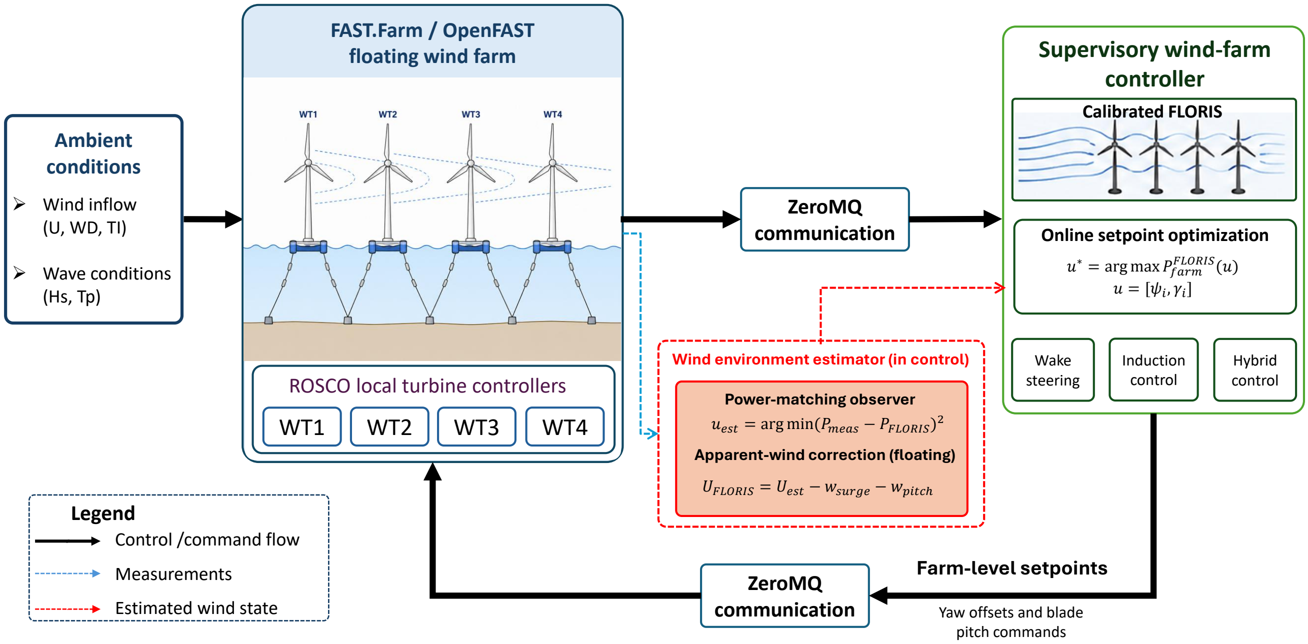

Figure 2. Closed-loop floating wind-farm control architecture. FAST.Farm resolves the floating wind-farm dynamics, ROSCO provides local turbine control, and the external FLORIS-based controller computes wake-steering, induction-control, or hybrid setpoints using turbine-level measurements exchanged through ZeroMQ.

2.5.2 FLORIS model and calibration

FLORIS is used as the supervisory engineering wake model for continuously computing farm-level control setpoints. In FLORIS, turbine wakes are represented using simplified and tunable engineering models, typically including a wake velocity-deficit model, a deflection model, a wake-added turbulence model and a wake superposition model (van Binsbergen et al., 2024). Because of their low computational cost, these analytical wake models are well suited for iterative applications such as online control optimization, where many model evaluations are required while meeting real-time constraints.

The FLORIS calibration procedure adopted in this work first consisted of generating turbine power and thrust lookup tables from OpenFAST simulations over the below-rated wind-speed range and for all derating setpoints considered. Each operating point was simulated for three hours of turbulent inflow, and the resulting time series were averaged to produce the lookup table entries. Because OpenFAST resolves the coupled aero-hydro-servo-elastic dynamics of the floating system, the resulting lookup tables inherently account for the effects of platform tilt, turbulent inflow, and controller response on the turbine power and thrust curves (Fontanella et al., 2023). Since the power curves are already parametrized on the tilt angle and the tilt effect on power is computed by OpenFAST rather than through empirical cosine-loss corrections, the tilt-induced power-loss exponent p_t was set to zero in the FLORIS configuration. The vertical wake deflection due to platform tilt is instead resolved by the FLORIS wake model, which accounts for its effect on the downstream flow field. The yaw-induced power-loss exponent

https://doi.org/10.5194/wes-2026-142
Preprint. Discussion started: 18 August 2026

was then calibrated to represent the reduction in turbine power under yaw-misaligned operation. Following the cosine-loss formulation commonly used in FLORIS-based wake-steering studies (Simley et al., 2021), the turbine power is expressed as

$$P = \frac{1}{2}\rho C_p A v^3 \cos^{p_P}(\gamma), \tag{1}$$

where ρ is the air density, C_P is the power coefficient obtained from the turbine lookup table, A is the rotor-swept area, v is the rotor-effective wind speed, γ is the yaw-misalignment angle, and p_P is the calibrated yaw power-loss exponent. No additional cosine correction associated with the turbine tilt angle is applied because the effect of the reference shaft tilt is already incorporated into the OpenFAST-derived power and thrust lookup tables.

The performance of the wind farm controller strongly depends on the accuracy of the engineering model with respect to the wind farm response (i.e., the FAST.Farm model here). In this work, the FLORIS model parameters are therefore calibrated prior to the controller synthesis, using FAST.Farm simulation data. Specifically, the power output of each wind turbine is computed, and the FLORIS wake model parameters are tuned to minimize the error in predicted power production. This calibration step enables FLORIS to provide more reliable setpoints during the subsequent control process, which is detailed later in this section. It is worth noting that the same calibration procedure can be applied using SCADA data from an operational wind farm, making this approach directly transferable to real power plants.

A first comparison between FAST.Farm and FLORIS under greedy control (baseline operation with zero yaw offsets and no induction action) showed a large mismatch. Since setpoints are computed by FLORIS and applied to the FAST.Farm plant, such mismatch would directly bias the optimal setpoints passed to the farm. In particular, FAST.Farm predicted stronger wake losses than FLORIS, and this discrepancy could not be resolved by solely using the power and thrust curves extracted from FAST.Farm to build the FLORIS model, indicating that the mismatch originates from differences in the wake and inflow modeling between the two frameworks.

The Gaussian curl hybrid (GCH) (King et al., 2021) model is adopted as the FLORIS wake model, as it is commonly used for wake-steering control applications. The calibration was carried out in three steps.

1. Turbine power and thrust lookup tables were generated from FAST.Farm simulations over the below-rated operating range and for the derating levels considered in this study. These lookup tables were then used in FLORIS to represent the turbine response under different derating setpoints.

2. The wake-deficit and wake-recovery behavior of the GCH model was adjusted to reproduce the turbine-level power predicted by FAST.Farm under greedy operation. In particular, the Gaussian wake-width function was modified as follows:

$$g(r) = C\exp\left(-\frac{r^n}{2\sigma^2}\right). \tag{2}$$

where r is the radial distance from the wake center, and C, n, and σ are parameters controlling the wake-deficit shape. A detailed description of the wake-deficit parametrization can be found in Annoni et al. (2018).

https://doi.org/10.5194/wes-2026-142
Preprint. Discussion started: 18 August 2026

eawe european academy of wind energy
Open Access WIND ENERGY SCIENCE DISCUSSIONS

Table 4. Main calibrated FLORIS parameters used in the supervisory controller for the three wind-direction cases considered in this study.

Parameter	$0°$	$-5°$	$-10°$
Gaussian wake-width parameter, σ	0.85	0.75	0.65
Near-wake length parameter, α	0.52	0.53	0.525
Wake-expansion parameter, k_a	-0.26	-0.17	-0.24
Wake-expansion parameter, k_b	0.06	0.057	0.074
Wake-deflection parameter, d_m	0.30	0.22	0.20
Wake-added turbulence parameter, a_i	0.30	0.50	0.30
Wake-added turbulence attenuation gain, G	0.30	0.30	0.30
Wake-added turbulence attenuation slope, S	3.5	3.5	3.5

3. The downstream evolution of the wake-added turbulence intensity was modified to reproduce the saturation-like behavior observed in FAST.Farm Branlard et al. (2024) for the third and fourth turbines. To address this, a rank-dependent attenuation factor was introduced in Bellini et al. (2026), defined as

$$\mathrm{TI}_i^+ = \mathrm{TI}_{i,\mathrm{base}}^+\, g(N_i), \tag{3}$$

where N_i is the number of upstream turbines affecting turbine i and $g(N_i)$ is an attenuation function that limits the cumulative turbulence addition in deep-array conditions:

$$g(N_i) = 1 - G\left(1 - e^{-SN_i}\right) \tag{4}$$

The parameters G and S were tuned to match the turbulence intensity levels predicted by FAST.Farm at the third and fourth turbine positions.

After matching the turbine-level power and turbulence-intensity trends under greedy operation, the wake deflection was calibrated using simulations with turbines subjected to prescribed yaw offsets. The uncalibrated FLORIS model overpredicted the wake deflection relative to FAST.Farm, so the deflection parameter was reduced. Since achieving satisfactory agreement with the FAST.Farm power predictions using a single tuned wake model was not feasible, the calibration procedure was repeated independently for the three wind directions considered, yielding a dedicated wake model for each case. The final calibrated values of the main FLORIS parameters are summarized in Table 4.

For a more detailed description of FLORIS and its wake-model formulations, the reader is referred to Bastankhah and Porté-Agel (2016); Niayifar and Porté-Agel (2016); King et al. (2021).

2.5.3 Observation of the wind environment

FLORIS is used not only as the supervisory wake model for farm-level setpoint optimization, but also as an estimator of the freestream wind speed. As shown in Figure 2, filtered turbine-power measurements are used to infer the wind speed that best matches the measured farm response.

https://doi.org/10.5194/wes-2026-142
Preprint. Discussion started: 18 August 2026

This strategy is adopted because similar observer-based formulations can also be extended to estimate additional inflow quantities, such as turbulence intensity and wind direction (Doekemeijer and van Wingerden, 2020; Doekemeijer et al., 2020). In the present implementation, the freestream wind speed is selected as the value that minimizes the squared error between the measured filtered power and the corresponding FLORIS prediction:

$$J(U) = [P_{\mathrm{farm}} - P_{\mathrm{FLORIS}}(U)]^2 \tag{5}$$

where P_{farm} is the filtered measured farm-power signal used by the observer and $P_{\mathrm{FLORIS}}(U)$ is the FLORIS-predicted farm power for a candidate freestream wind speed U. The FLORIS prediction is evaluated over the wind-speed interval $U \in [5, 13]\,\mathrm{m\,s^{-1}}$, discretized into 121 equally spaced candidate values, corresponding to a step size of approximately $0.067\,\mathrm{m\,s^{-1}}$.

In this work, a moving average filter with a window of $50\,\mathrm{s}$ is applied to all turbine-level signals transmitted by FAST.Farm to the farm controller, including power, thrust, platform motions, and nacelle orientation, before they are used for wind speed estimation and setpoint computation. To account for platform motion in floating conditions, the estimation is extended by including the relative wind speed induced by surge and pitch velocities at hub height. The surge and pitch contributions are estimated from finite differences over the same averaging window, before passing it to FLORIS, as expressed in Equations (6) and (7):

$$w_{\mathrm{surge}} = \frac{\Delta X_{\mathrm{surge}}}{\Delta T} \tag{6}$$

$$w_{\mathrm{pitch}} = \frac{\sin(\Delta\theta) \cdot h_{\mathrm{hub}}}{\Delta T} \tag{7}$$

where w_{surge} and w_{pitch} are the contributions of the platform surge displacement change $\Delta X_{\mathrm{surge}}$ and pitch rotation change $\Delta\theta$ over the averaging window ΔT to the apparent wind speed at hub height, respectively. The wind-speed input supplied to FLORIS is then

$$U_{\mathrm{FLORIS}} = U_{\mathrm{est}} - w_{\mathrm{surge}} - w_{\mathrm{pitch}}, \tag{8}$$

where U_{est} is the wind speed obtained from the power-matching procedure. Without this correction, the wind-speed input to FLORIS would be biased by the omitted apparent-wind term $w_{\mathrm{surge}} + w_{\mathrm{pitch}}$. Although this term is small compared with the mean inflow speed, it is relevant for below-rated control because the FLORIS power prediction is sensitive to wind-speed variations. The resulting wind-speed-estimation accuracy is assessed in Section 3.

2.5.4 Farm control strategies

Four wind farm control strategies are compared in this study: greedy baseline operation, wake steering, induction control, and hybrid control. The greedy strategy is used as the reference for the relative power and fatigue-load comparisons unless

https://doi.org/10.5194/wes-2026-142
Preprint. Discussion started: 18 August 2026

otherwise stated. In the three strategies controlling the wind farm flow, setpoints are computed using the calibrated FLORIS model and then applied to FAST.Farm through the closed-loop controller interface described in Section 2.5.

2.5.5 Greedy baseline control

In the greedy baseline strategy, each turbine is controlled independently by ROSCO to maximize its own power production, without considering its effects on downstream turbines. No farm-level yaw-misalignment or derating commands are applied; therefore, the yaw-offset and pitch-offset setpoints are set to zero. Under the investigated below-rated wind conditions, each turbine follows its standard maximum-power-point control strategy. This operating mode is used as the reference for all power, platform-motion, and fatigue-load comparisons.

2.5.6 Wake steering control

The wake-steering strategy is implemented by computing yaw setpoints in FLORIS using the Serial-Refine method of Fleming et al. (2022), which effectively balances computational speed and accuracy. In this work, the yaw angle range was limited to $[-20°, 20°]$. This choice is supported by studies showing that wake deflection increases approximately linearly up to about 20°, while further deflections (and power gains of downstream turbines) between 20° and 30° are marginal and are accompanied by a substantial increase in loads (Nash et al., 2021) for the turbine applying the yaw offset.

The Serial-Refine algorithm used for yaw angle optimization relies on the assumption that the yaw setting of a downstream turbine does not affect the power of the turbines upstream of it, which allows the optimization to be decoupled and solved sequentially. It proceeds in two stages. In the *Serial* stage, the yaw setpoint range is discretized into a user-defined set of candidate angles; starting from the most upstream turbine, each candidate yaw value is applied in turn, the total farm power is evaluated, and the angle yielding the highest power is retained. This is repeated for each turbine in the farm moving downstream, with the most downstream turbine fixed at zero yaw, as it has no downstream wakes to steer. In the subsequent *Refine* stage, the yaw setpoint search interval is narrowed around the angle selected in the *Serial* stage and the same procedure of the *Serial* stage is repeated.

The number of refinement steps, the interval width, and its discretization are user-defined parameters. In this work, two refinement steps were used: the initial yaw interval spanned $[-20°, 20°]$ discretized into 11 candidate angles. A second pass then searched a narrower interval around the angle selected during the first pass using four candidate values.

2.5.7 Induction control

The induction control strategy is implemented by derating selected turbines through blade-pitch offsets. To represent derated operation in FLORIS, separate turbine-performance lookup tables were generated for each admissible derating level. Eleven discrete derating levels were considered, indexed as $d_i \in \{0, 1, \ldots, 10\}$, where $d_i = 0$ corresponds to the non-derated turbine and larger values of d_i correspond to increasing blade-pitch offsets and stronger derating.

https://doi.org/10.5194/wes-2026-142
Preprint. Discussion started: 18 August 2026

WIND ENERGY SCIENCE DISCUSSIONS

For each derating level, a separate turbine-performance table was provided to FLORIS as a distinct turbine definition. These tables contain the corresponding C_p, C_t, and floating-platform tilt data. During the induction-control optimization, FLORIS evaluates a candidate derating vector $\mathbf{d}$ by assigning to each turbine the lookup table associated with its selected derating level d_i. In this way, the optimizer accounts for the effect of blade-pitch-based derating on both farm power and rotor thrust.

The derating setpoints are selected using a discrete sequential search similar in spirit to the Serial-Refine approach (Fleming et al., 2022). Candidate derating levels are tested in FLORIS, and the configuration providing the highest predicted farm power while satisfying the farm-level rotor-thrust constraint is retained. The selected derating indices are then converted into the corresponding blade-pitch offsets and transmitted to FAST.Farm through the ROSCO wind-farm-control interface.

The effectiveness of induction control depends on the strength of the wake interactions, turbine spacing, atmospheric conditions, and turbine operating characteristics. Its effects are generally more pronounced for closely spaced and aligned turbines, where upstream derating can weaken the wake and increase the power available to downstream machines; however, the downstream recovery may not fully compensate for the power sacrificed by the derated turbines (Houck and Cowen, 2022; Bossanyi and Ruisi, 2021). Therefore, a maximum acceptable farm-level rotor-thrust ratio is imposed in the present optimization to bound the aggregate aerodynamic rotor thrust used as a load-related proxy.

The discrete derating levels are defined as

$$d_i \in D = \{0, 1, 2, \ldots, 10\}, \tag{9}$$

where d_i is the derating level assigned to turbine i, and D is the discrete set of admissible levels. The vector $\mathbf{d} = \{d_1, d_2, \ldots, d_N\}$ collects the derating setpoints applied to the N turbines of the farm.

For a given wind speed w_s and wind direction w_d, the farm power and farm rotor thrust are defined as

$$\begin{aligned} P(\mathbf{d}; w_s, w_d) &= \sum_{i=1}^{N} P_i(\mathbf{d}; w_s, w_d), \\ T(\mathbf{d}; w_s, w_d) &= \sum_{i=1}^{N} T_i(\mathbf{d}; w_s, w_d). \end{aligned} \tag{10}$$

The rotor thrust of each turbine is computed as

$$T_i(\mathbf{d}; w_s, w_d) = \tfrac{1}{2}\,\rho\, C_{t,i}(d_i)\, A\, v_i^2 \cos^{p_p}(\gamma_i)\cos^{p_t}(\zeta_i), \tag{11}$$

where $C_{t,i}(d_i)$ is obtained from the FLORIS lookup table associated with the selected derating level, A is the rotor-swept area, v_i is the effective wind speed at turbine i, γ_i is the yaw offset, and ζ_i is the tilt angle. For the induction-only controller, $\gamma_i = 0$, whereas the same thrust expression is later used for the hybrid controller with nonzero yaw offsets.

The baseline power and thrust are computed at $\mathbf{d} = \mathbf{0}$, corresponding to non-derated operation on all turbines. These quantities are used to define the relative farm power and farm thrust:

https://doi.org/10.5194/wes-2026-142
Preprint. Discussion started: 18 August 2026

$$P_{\mathrm{rel}}(\mathbf{d}) = \frac{P(\mathbf{d})}{P_{\mathrm{base}}}, \qquad T_{\mathrm{rel}}(\mathbf{d}) = \frac{T(\mathbf{d})}{T_{\mathrm{base}}}. \tag{12}$$

The constrained derating optimization is then formulated as

$$\begin{aligned} \mathbf{d}^{\star} \in \arg\max_{\mathbf{d}\in D^N} & \; P_{\mathrm{rel}}(\mathbf{d}) \\ \text{s.t. } & T_{\mathrm{rel}}(\mathbf{d}) \le \gamma_{\mathrm{thrust}}, \end{aligned} \tag{13}$$

where $\gamma_{\mathrm{thrust}} = 0.9$. Since the derating setpoints are drawn from the discrete set D, the problem is solved by sequentially sweeping over the candidate derating levels for each turbine, similarly to the discretized yaw-angle search used in the Serial-Refine strategy (Fleming et al., 2022). Each candidate is evaluated in FLORIS, and the feasible candidate that maximizes P_{rel} is retained.

In the implemented sequential search, the procedure starts from a strongly derated configuration for the upstream turbines and progressively relaxes the derating level to increase farm power while satisfying the thrust constraint. The most downstream turbine is fixed at $d = 0$ throughout the search, because its derating cannot provide a wake-recovery benefit to any downstream machine. For $k = 1, \ldots, N-1$, each admissible derating level $d_{i_k} \in D$ is tested while keeping the levels already selected for the previous turbines fixed. At each trial, the farm power and thrust are recomputed in FLORIS and evaluated according to

$$\begin{aligned} & T_{\mathrm{rel}}(\mathbf{d}) \le \gamma_{\mathrm{thrust}} \quad \text{(thrust constraint)}, \\ & J(\mathbf{d}) = P_{\mathrm{rel}}(\mathbf{d}) \quad \text{(objective to maximize)}. \end{aligned} \tag{14}$$

The derating level that maximizes J among the feasible candidates is selected. Formally, at search step k,

$$d^{\star}_{i_k} \in \arg\max_{d\in D} \left\{ P_{\mathrm{rel}}\left(\mathbf{d}^{(k-1)}[i_k \leftarrow d]\right) : T_{\mathrm{rel}}\left(\mathbf{d}^{(k-1)}[i_k \leftarrow d]\right) \le \gamma_{\mathrm{thrust}} \right\}, \tag{15}$$

where $\mathbf{d}^{(k-1)}[i_k \leftarrow d]$ denotes the candidate vector obtained by assigning level d to turbine i_k while keeping the previously selected levels unchanged. At the end of the procedure, a feasible configuration $\mathbf{d}^{\star}$ satisfying $T_{\mathrm{rel}} \le \gamma_{\mathrm{thrust}}$ is obtained.

2.5.8 Hybrid wake steering–derating control

The hybrid strategy combines wake steering and induction control to increase farm power while limiting the aerodynamic rotor thrust of the wind farm. The yaw and derating setpoints are updated sequentially and are then applied simultaneously to the turbine controllers.

This ordering is chosen because wake steering primarily determines the wake topology seen by the downstream turbines. The yaw offsets modify the wake deflection, wake overlap, and effective inflow velocities throughout the farm; therefore, the aerodynamic effect of a given derating vector depends on the yawed operating state. By optimizing yaw first, the controller establishes the wake-redirection condition that maximizes the FLORIS-predicted power. The derating stage is then applied on top of this yawed condition to reduce the farm rotor thrust while preserving as much of the wake-steering power gain

https://doi.org/10.5194/wes-2026-142
Preprint. Discussion started: 18 August 2026

as possible. This sequential formulation avoids the computational cost of a fully joint yaw–derating optimization while still accounting for the dominant coupling between the two control actions.

At control update k, the wake-steering optimization is first performed using turbine models corresponding to the derating levels selected at the previous update. Accordingly, the yaw-angle vector can be expressed as

$$\gamma_k^\star = \arg\max_{\boldsymbol{\gamma}} P_{\text{farm}}\left(\boldsymbol{\gamma}, \boldsymbol{d}_{k-1}\right), \tag{16}$$

where $\boldsymbol{\gamma}$ denotes the turbine yaw-offset vector and $\boldsymbol{d}$ denotes the discrete derating-level vector.

The derating optimization is then carried out using the newly computed yaw solution. The derating vector is selected as

$$\boldsymbol{d}_k^\star = \arg\max_{\boldsymbol{d} \in D^N} P_{\text{farm}}\left(\gamma_k^\star, \boldsymbol{d}\right), \tag{17}$$

subject to the farm-level rotor-thrust constraint

$$\frac{T_{\text{farm}}\left(\gamma_k^\star, \boldsymbol{d}\right)}{T_{\text{farm}}\left(\gamma_k^\star, \boldsymbol{0}\right)} \le \gamma_{\text{thrust}}, \qquad \gamma_{\text{thrust}} = 0.9. \tag{18}$$

Thus, in the hybrid controller, the derating constraint is imposed relative to the non-derated yawed FLORIS condition, rather than relative to the zero-yaw greedy condition. The resulting derating levels are converted into collective blade-pitch offsets, and the final yaw and pitch commands, $\gamma_k^\star$ and $\boldsymbol{\beta}_k^\star$, are transmitted simultaneously to the turbine controllers.

The hybrid strategy is therefore sequential rather than fully joint: the yaw optimization uses the previously selected derating state, and the subsequent derating optimization uses the newly optimized yaw state. This implementation captures part of the coupling between wake steering and derating while remaining computationally suitable for online control.

3 Results

Unless otherwise stated all results reported in this section are obtained from the FAST.Farm simulations. FLORIS is used to determine the farm-level control setpoints but is not used to calculate the reported performance metrics.

3.1 Free-stream wind speed estimation

An accurate estimation of the state of the wind farm is crucial for the effectiveness of the proposed control framework. This capability was tested under turbulent inflow with 6% turbulence intensity and a mean wind speed of $8\ \mathrm{m\,s^{-1}}$.

https://doi.org/10.5194/wes-2026-142
Preprint. Discussion started: 18 August 2026

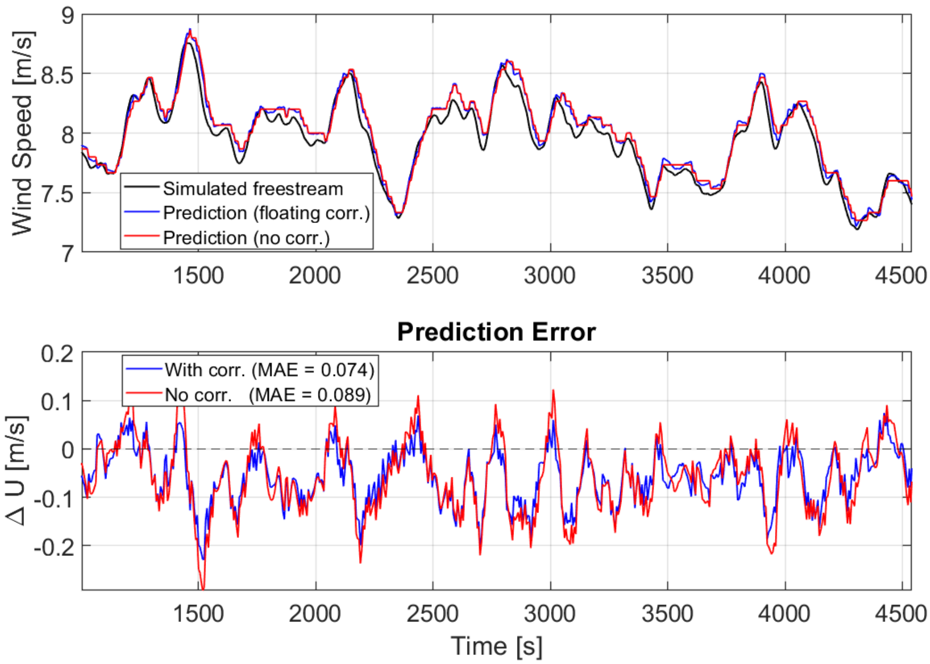

Figure 3. Performance of the FLORIS-based wind-speed observer. The comparison between the simulated freestream wind speed and the wind speed estimated using the FLORIS-based observer for the representative $8\ \mathrm{m\,s^{-1}}$ turbulent inflow case (greedy baseline), excluding the initial transient ($t \geq 1000$ s). The upper panel shows the time histories; the lower panel shows the prediction error with and without the floating platform motion correction.

The prediction follows the main low-frequency variations of the simulated wind speed throughout the analysed period. When the floating correction (platform pitch velocity at hub height plus surge velocity) is included, the mean absolute error is $0.065\ \mathrm{m\,s^{-1}}$, the root-mean-square error is $0.080\ \mathrm{m\,s^{-1}}$, and the mean bias is $-0.058\ \mathrm{m\,s^{-1}}$, with a maximum absolute error of $0.228\ \mathrm{m\,s^{-1}}$. These values correspond to approximately 0.8%, 1.0%, 0.7%, and 2.9% of the nominal $8\ \mathrm{m\,s^{-1}}$ inflow speed, respectively. Without the floating correction, the corresponding figures increase to $0.076\ \mathrm{m\,s^{-1}}$ (1.0%), $0.094\ \mathrm{m\,s^{-1}}$ (1.2%), $-0.058\ \mathrm{m\,s^{-1}}$ (0.7%), and $0.292\ \mathrm{m\,s^{-1}}$ (3.7%). The floating motion compensation therefore reduces the MAE by approximately 14% and the peak error by 22%, confirming that accounting for platform kinematics improves the wind speed estimate fed to the FLORIS-based setpoint optimiser.

3.2 Control actuation and turbine–platform response

Figure 4 compares the relative changes in the mean and standard deviation of the total farm-power signal with respect to the matched greedy baseline. The upper row shows that all three control strategies increase mean farm power for every investigated wind speed and wind direction. The largest gains are obtained using induction and hybrid control, particularly at $WD = -5°$,

https://doi.org/10.5194/wes-2026-142
Preprint. Discussion started: 18 August 2026

eawe european academy of wind energy
Open Access WIND ENERGY SCIENCE DISCUSSIONS

where the increase reaches approximately 19% at $8\ \mathrm{m/s}$. Under the same alignment, wake steering provides a considerably smaller improvement of approximately 1.6%–2.9%.

The limited benefit of wake steering at $WD = -5°$ is consistent with the relatively small farm-averaged nacelle-yaw angles shown in Figure 5, which range from approximately $4.20°$ to $6.26°$. The resulting lateral wake displacement is insufficient to eliminate the overlap between the wake cores and the downstream rotors. Consequently, the downstream power recovery only partly compensates for the power loss of the yaw-misaligned upstream turbines.

Across the complete operating matrix, hybrid control provides the highest or near-highest mean farm-power gain. At $WD = 0°$, its gain exceeds that of induction control by approximately 3.1%–4.0%, whereas the additional benefit at $WD = -10°$ ranges from approximately 0.9% to 2.0%. At $WD = -5°$, induction and hybrid control provide almost identical gains, with differences below 0.7%. This indicates that pitch-based induction control is the main contributor under the strongest wake-interaction condition, while yaw-based wake redirection provides an additional benefit mainly at $WD = 0°$ and $WD = -10°$.

The lower row reveals that the corresponding farm-power variability depends strongly on wind direction. At $WD = 0°$, induction control reduces the farm-power standard deviation by 2.7%–4.7%, while hybrid control produces changes between $+0.1\%$ and -2.7%. These strategies therefore increase mean farm power without increasing, and generally while reducing, the variability of the aggregate farm output. Wake steering also produces only small changes in this condition.

At $WD = -5°$, the increases in mean power are accompanied by greater farm-power variability. Induction and hybrid control increase the farm-power standard deviation by approximately 1.2%–4.5% and 4.0%–11.1%, respectively. Wake steering provides the least favorable compromise: its mean-power gain remains below 3%, whereas the standard deviation increases by 13.1% at $7\ \mathrm{m/s}$ and 8.4% at $8\ \mathrm{m/s}$.

At $WD = -10°$, induction and hybrid control again provide a more favorable balance than wake steering. Their variability changes remain small at 7 and $9\ \mathrm{m/s}$ and decrease by approximately 5% at $8\ \mathrm{m/s}$. Wake steering, in contrast, increases the farm-power standard deviation by 5.2%–9.4% while providing smaller mean power gains. Overall, the results demonstrate that controller performance should be evaluated in terms of both mean farm power and the steadiness of the total farm output.

https://doi.org/10.5194/wes-2026-142
Preprint. Discussion started: 18 August 2026

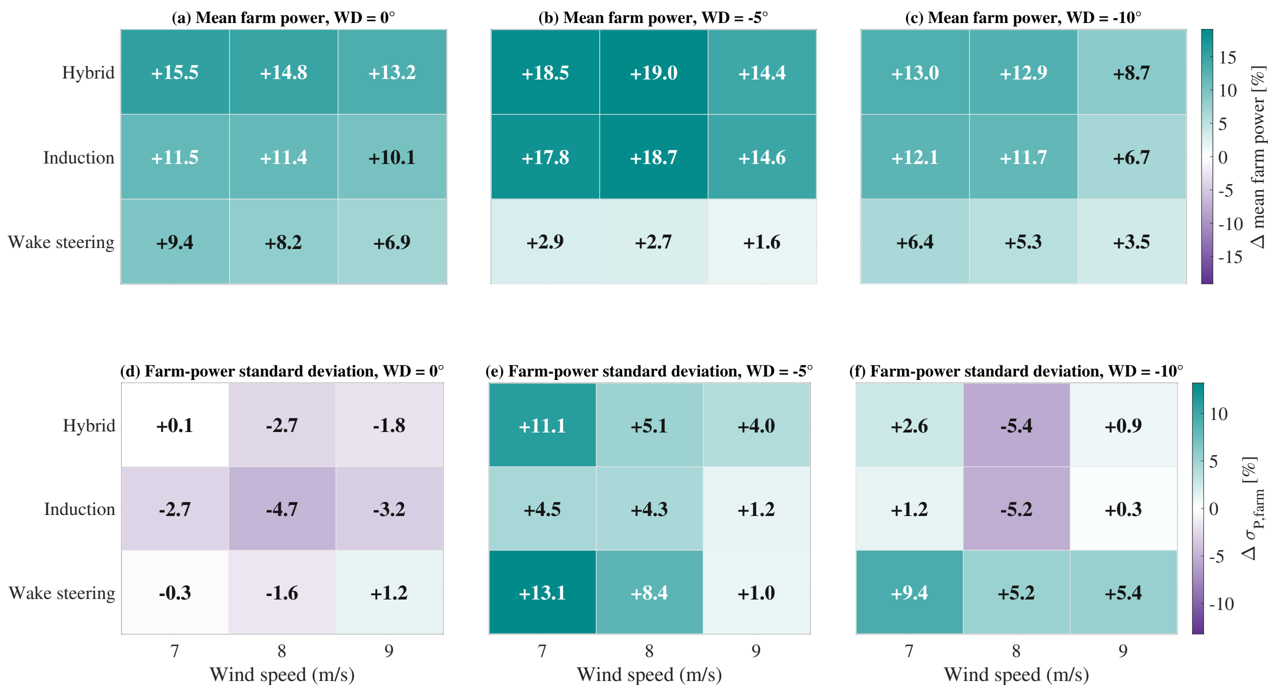

Figure 4. Farm-power mean and variability response. Relative changes in the mean and standard deviation of the total farm-power signal with respect to the matched greedy baseline. Panels (a)–(c) show the mean farm-power changes for $WD = 0°$, $-5°$, and $-10°$, respectively, while panels (d)–(f) show the corresponding changes in farm-power standard deviation. The instantaneous farm power is obtained by summing the generator-power signals of the four turbines before calculating its mean and standard deviation. Each relative change is evaluated against the greedy case with the same wind speed, wind direction, and turbulent seed, and the displayed values are averaged over the five seeds. Positive values in the upper row indicate increased mean farm power, whereas positive and negative values in the lower row indicate increased and reduced farm-power variability, respectively.

Figure 5 shows the farm-averaged realized nacelle-yaw and collective blade-pitch angles for the four operating strategies. These values are not identical to the turbine-specific offsets generated by the supervisory controller. The farm-level commands are passed to the independent ROSCO controllers, while the final nacelle orientation and blade-pitch angles result from the internal ROSCO control loops, actuator dynamics, and coupled turbine–platform response.

Wake steering acts primarily through nacelle yaw and produces the largest realized yaw angles among the investigated strategies. The mean yaw angle is positive at $WD = 0°$ and $WD = -5°$, reaching approximately $12.60°$ at $WD = 0°$, whereas it becomes negative at $WD = -10°$ because the favorable wake-deflection direction reverses with the farm–wake alignment. At $WD = -5°$, the realized farm-averaged yaw angles remain relatively small, approximately $4.20°$–$6.26°$, and produce only limited wake displacement. This is consistent with the modest farm-power gains of approximately 1.6–2.9 %, because the downstream recovery only partly compensates for the power loss of the yaw-misaligned upstream turbines.

https://doi.org/10.5194/wes-2026-142
Preprint. Discussion started: 18 August 2026

Induction control applies zero farm-level yaw offset and acts through pitch-based derating. Its realized nacelle-yaw angles therefore remain close to those of greedy operation, while the collective blade-pitch angle increases, particularly at $WD = -5°$ and $WD = -10°$, where farm-averaged values of approximately 3°–4° are obtained. These pitch settings reduce power extraction and rotor thrust at selected upstream turbines, thereby weakening their wakes and increasing the power available to several downstream turbines. The resulting downstream recovery explains why induction control achieves substantially larger farm-power gains than wake steering under the strongly waked $WD = -5°$ condition.

The hybrid controller combines nonzero yaw action with pitch-based derating setpoints computed after the yaw optimization. Its power gains therefore arise from the combined effect of wake redirection and wake weakening. The relative importance of the two mechanisms depends on wind direction: yaw redirection is more beneficial when wake steering produces a meaningful lateral displacement, whereas pitch-based derating remains dominant under the most strongly waked conditions.

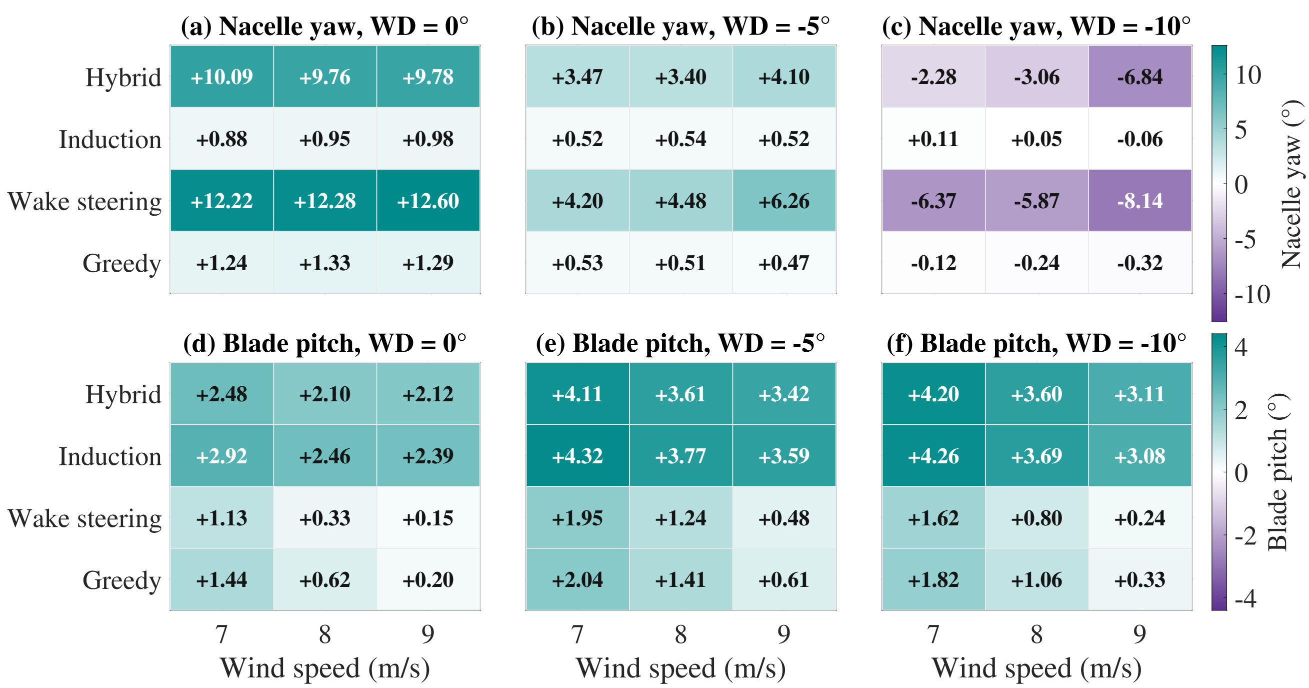

Figure 5. Realized nacelle-yaw and blade-pitch response. Farm-averaged realized nacelle-yaw and collective blade-pitch responses for the four operating strategies. Panels (a)–(c) show the nacelle-yaw angles for $WD = 0°$, $WD = -5°$, and $WD = -10°$, respectively, while panels (d)–(f) show the corresponding blade-pitch angles. Within each panel, the columns represent wind speeds of (7), (8), and 9 $\mathrm{m/s}$, and the rows represent hybrid control, induction control, wake steering, and greedy operation. The values are computed after removal of the initial transient and are averaged over the four turbines and five turbulent realizations. The plotted quantities are the realized turbine responses and therefore do not necessarily coincide exactly with the turbine-specific yaw and pitch-offset commands generated by the supervisory controller.

Figure 6 is included because the nacelle-yaw quantity reported in Figure 5 is measured relative to the moving floating platform. The platform itself undergoes a yaw rotation, and therefore the realized rotor orientation in the global reference frame

https://doi.org/10.5194/wes-2026-142
Preprint. Discussion started: 18 August 2026

eawe european academy of wind energy
Open Access WIND ENERGY SCIENCE DISCUSSIONS

depends on both the nacelle-yaw angle and the platform-yaw response. Examining platform yaw is consequently necessary to distinguish the controller-imposed nacelle rotation from the additional rotation of the floating support structure.

At $WD = 0°$, the mean platform-yaw angle is negative for all strategies. Wake steering produces the largest response, increasing in magnitude from $-1.03°$ at $7\ \mathrm{m/s}$ to $-1.25°$ at $9\ \mathrm{m/s}$. The greedy, hybrid, and induction cases show smaller negative rotations, with induction producing the smallest magnitude. At $WD = -5°$, the platform response is much smaller for greedy and induction operation, remaining close to zero, whereas wake steering still produces a substantial negative rotation of approximately $-0.66°$ to $-0.78°$. At $WD = -10°$, the platform-yaw angle changes sign and becomes positive for all strategies. Wake steering again gives the largest response, reaching $1.30°$ at $9\ \mathrm{m/s}$, while the induction, greedy, and hybrid cases remain below approximately $0.7°$. These results show that wake steering generates the strongest platform-yaw response and that platform motion provides a non-negligible contribution to the effective turbine orientation.

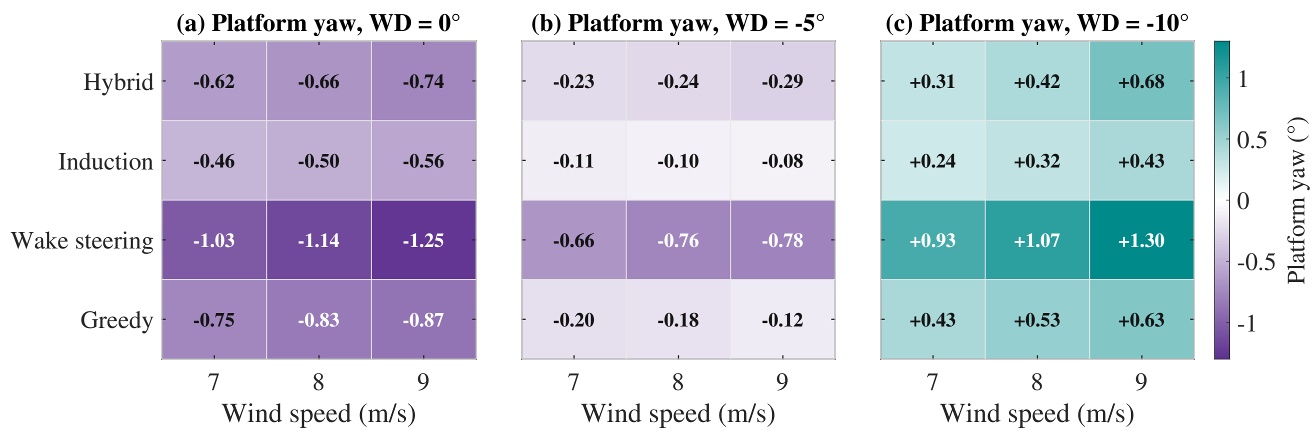

Figure 6. Floating-platform yaw response. Farm-average platform-yaw angle for the greedy, wake-steering, induction-control, and hybrid cases. Panels (a), (b), and (c) correspond to inflow directions $WD = 0°$, $-5°$, and $-10°$, respectively. In each panel, the columns represent wind speeds of 7, 8, and 9 $\mathrm{m/s}$, while the rows represent the four control strategies. For each FAST.Farm case, the mean platform-yaw angle is first averaged over the four turbines and subsequently averaged over the five turbulent seeds. Negative and positive values indicate platform rotation in opposite yaw directions. The results highlight the contribution of floating-platform motion to the realized turbine orientation, particularly under wake-steering control.

Although the greedy and wake-steering controllers apply zero external blade-pitch offset, the actual blade-pitch angle is not identically zero. The upstream turbine, T1, remains close to its fine-pitch operating condition for nearly all cases, whereas the downstream turbines exhibit positive mean blade pitch, particularly at $7\ \mathrm{m/s}$, where the wake-induced velocity deficit is strongest. The largest downstream values approach approximately $3°$.

The non-zero blade pitch originates from the turbine-level controller rather than from the wind-farm controller. Under strongly waked conditions, the rotor-averaged axial velocity decreases while the rotor speed approaches its lower operating plateau. Consequently, the rotor tip-speed ratio increases and its increment is strongly correlated with positive blade pitch. This behavior is consistent with the low-wind minimum-pitch schedule applied by the turbine-level controller. Wake steering

https://doi.org/10.5194/wes-2026-142
Preprint. Discussion started: 18 August 2026

eawe european academy of wind energy
Open Access WIND ENERGY SCIENCE DISCUSSIONS

generally reduces the blade pitch of downstream turbines relative to greedy operation by partially recovering the local inflow and moving the downstream turbines away from this low-velocity, high-tip-speed-ratio operating region, as shown in Figure 7.

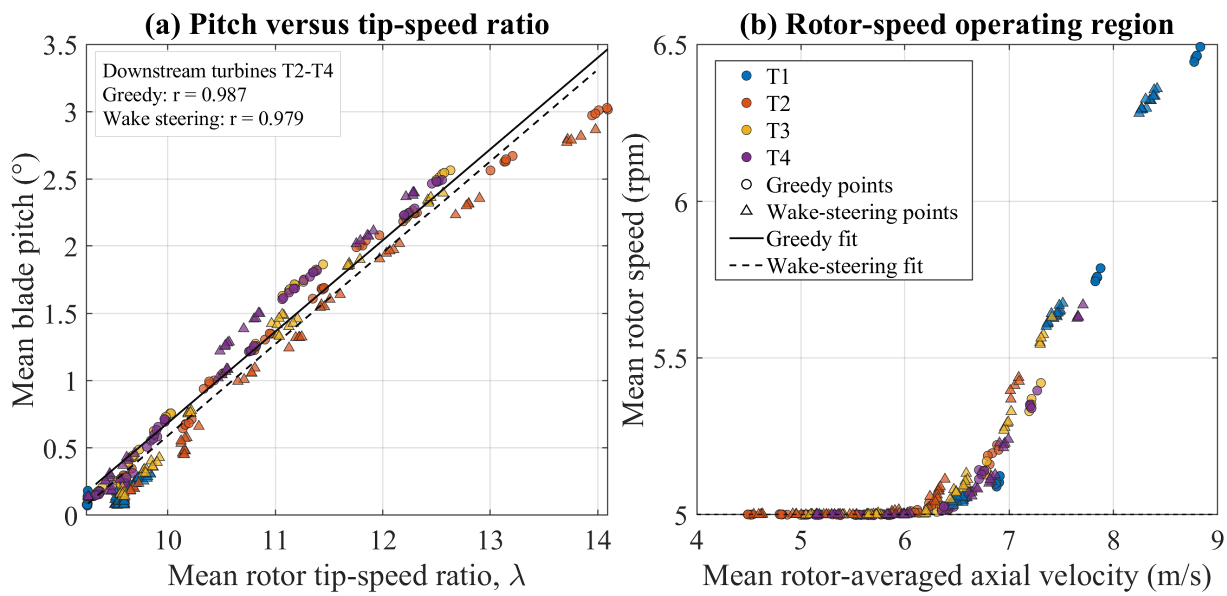

Figure 7. Origin of the nonzero blade-pitch response. Turbine-level operating conditions associated with the nonzero blade pitch under greedy and wake-steering operation. Panel (a) shows the mean blade-pitch angle as a function of the mean rotor tip-speed ratio. The solid and dashed lines are least-squares fits for the downstream turbines T2–T4 under greedy and wake-steering operation, respectively, and r denotes the Pearson correlation coefficient. Panel (b) shows the mean rotor speed as a function of the mean rotor-averaged axial velocity; the horizontal dashed line indicates the observed low-speed rotor-speed plateau. Marker color identifies the turbine, while marker shape identifies the control strategy. Each point represents one turbine, turbulent seed, and operating case after removal of the initial transient.

3.3 Rotor-thrust response

The derating-based controllers include a FLORIS-level farm rotor-thrust constraint. To verify how this constraint is reflected in the dynamic FAST.Farm simulations, the mean rotor thrust was post-processed from the OpenFAST `RotThrust` channel. The normalization follows the reference condition used by the controller optimization. Wake steering and induction control are reported relative to the matched greedy case, whereas hybrid control is reported relative to the matched wake-steering case. This choice reflects the fact that induction control constrains derated operation relative to the non-derated zero-yaw FLORIS baseline, while hybrid control constrains derated operation relative to the non-derated yawed FLORIS condition.

Figure 8 shows that induction control generally reduces the farm-level mean rotor thrust relative to greedy operation. The hybrid controller similarly reduces the mean farm rotor thrust relative to the wake-steering operating point, confirming that the added derating stage partly unloads the farm after yaw optimization. Differences from the imposed 0.9 FLORIS threshold are

https://doi.org/10.5194/wes-2026-142
Preprint. Discussion started: 18 August 2026

expected because the constraint is applied in the steady-state FLORIS optimizer, whereas the plotted values are obtained from turbulent, dynamic FAST.Farm simulations.

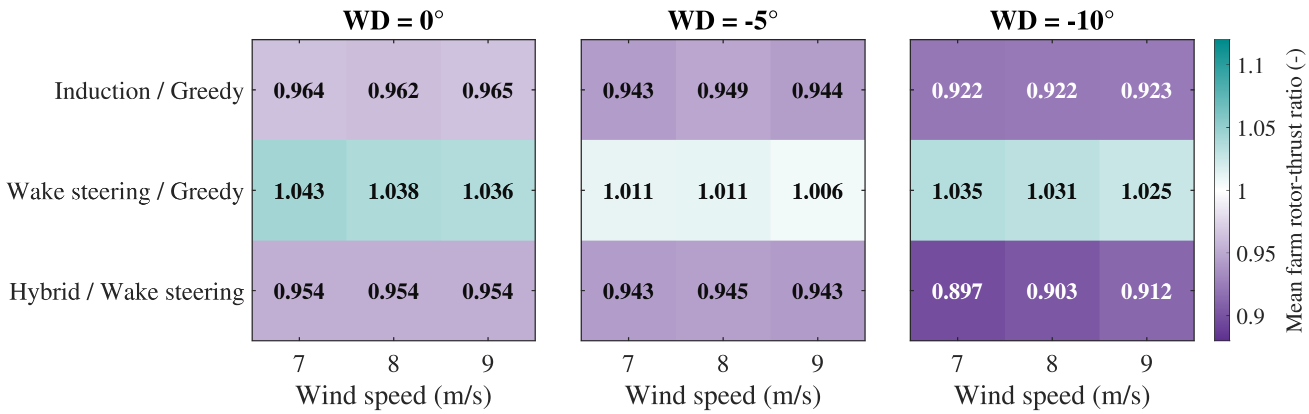

Figure 8. Farm-level rotor-thrust response. Seed-averaged farm-level mean rotor-thrust ratio. Wake steering and induction control are normalized by the matched greedy baseline, whereas hybrid control is normalized by the matched wake-steering case. This normalization follows the reference condition used in the derating optimization: induction constrains the derated farm thrust relative to the non-derated zero-yaw FLORIS baseline, while hybrid constrains the derated farm thrust relative to the non-derated yawed FLORIS condition. Values below unity indicate reduced mean farm rotor thrust relative to the corresponding reference.

Wake steering alone generally increases the mean farm rotor thrust relative to greedy operation, with ratios slightly above unity. This increase is a consequence of the yawed operating state and the resulting redistribution of rotor loading. In contrast, induction control reduces the mean farm rotor thrust relative to greedy operation for all investigated conditions. The hybrid controller also reduces the mean farm rotor thrust relative to the corresponding wake-steering case, confirming that the derating stage introduces additional aerodynamic unloading after yaw optimization. The largest hybrid reduction occurs at $WD = -10°$, where the ratio decreases to approximately 0.90.

The realized ratios do not necessarily coincide with the imposed $\gamma_{\mathrm{thrust}} = 0.9$ threshold, because the constraint is applied inside the steady-state FLORIS optimization, whereas the plotted values are computed from the dynamic turbulent FAST.Farm simulations. Therefore, the threshold should be interpreted as a controller-design constraint rather than as an exact target for the realized FAST.Farm mean thrust.

3.4 Farm-level fatigue-load response

For the farm-level load comparison, a conservative DEL envelope is used. For every wind speed, wind direction, turbulent seed, and control strategy, the farm-level DEL is defined as the maximum turbine-level DEL among the four turbines. This procedure prevents a local fatigue-load increase at one turbine from being obscured by reductions at other turbines. For the mooring response, one fairlead line is selected separately for each turbine as the line exhibiting the largest mean absolute controller-induced DEL variation among the three fairlead lines. The same selected line is used consistently for the matched greedy and controlled cases, thereby avoiding an artificial signal caused by switching between fairlead lines. The turbine-level mooring quantity is then defined as the DEL of this selected fairlead-line tension, and the corresponding farm-level value is obtained by taking the maximum over the four turbines.

Figure 9 shows that the farm-level fatigue response is strongly dependent on the selected load channel. The blade-root bending-moment DEL in panel (a) is generally reduced by induction and hybrid control. The largest reductions occur at the higher wind speeds for $WD = 0°$ and $WD = -5°$. Wake steering produces a different response at $WD = -10°$, where the blade-root DEL increases, reaching its largest increase at $9\ \mathrm{m/s}$.

The tower-base bending-moment DEL in panel (b) exhibits a less uniform response. The largest increases occur at $WD = -5°$, particularly at $9\ \mathrm{m/s}$, where induction and hybrid control increase the farm-level DEL by approximately 40%. Substantial increases are also observed at $WD = -10°$ and $9\ \mathrm{m/s}$, whereas the changes are smaller or negative for several $WD = 0°$ and lower-wind-speed cases. These results indicate that the tower-base fatigue response is highly dependent on the operating condition.

The most systematic controller dependence is observed for the selected yaw-bearing bending moment DEL in panel (c). Wake steering increases this DEL for every investigated condition, with changes of approximately 8%–20%. In contrast, induction and hybrid control reduce the yaw-bearing moment DEL for all conditions, with reductions approaching 30% in several cases. Among the four evaluated load channels, the selected yaw-bearing moment therefore exhibits the clearest and most consistent dependence on the control strategy.

The critical fairlead-line tension DEL in panel (d) is more condition-dependent. Induction and hybrid control generally reduce the fairlead DEL at $WD = 0°$, but produce substantial increases at $WD = -5°$, particularly at 7 and $9\ \mathrm{m/s}$. Increases are also observed at $WD = -10°$ and $9\ \mathrm{m/s}$. These results demonstrate that the mooring fatigue response is sensitive to wind direction, wind speed, and control strategy.

https://doi.org/10.5194/wes-2026-142
Preprint. Discussion started: 18 August 2026

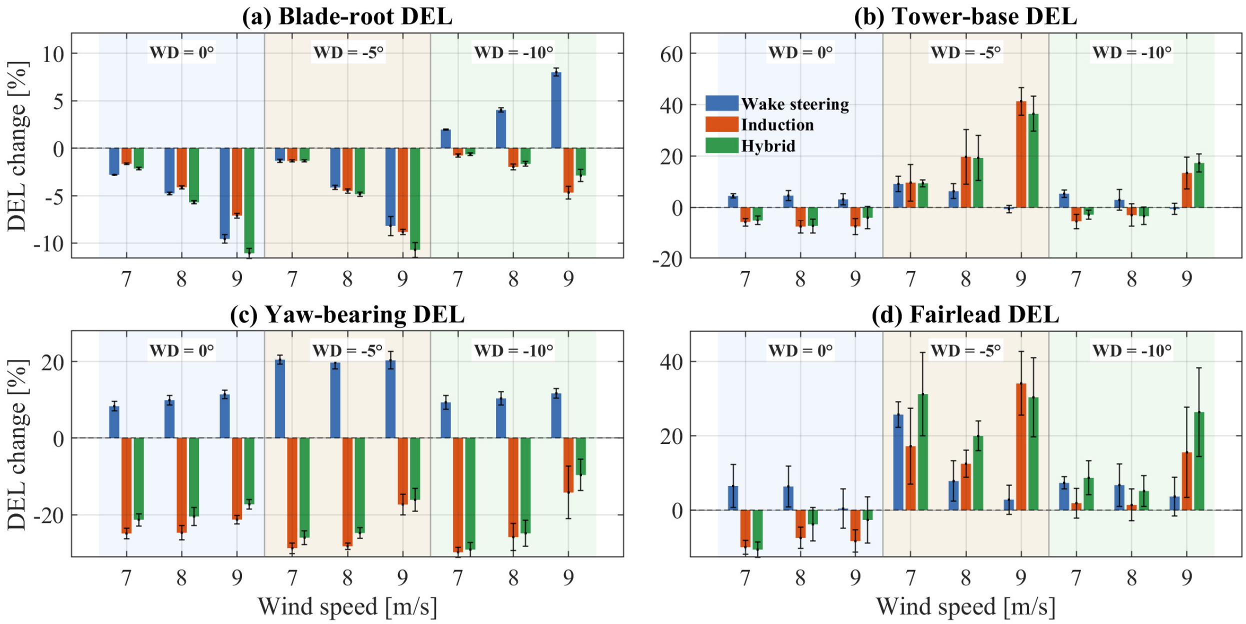

Figure 9. Farm-level fatigue-load response. Relative changes in the DELs of the selected blade-root bending moment, tower-base bending moment, yaw-bearing moment, and critical fairlead-line tension relative to the matched greedy baseline. Panels (a)–(d) show the relative changes in the DELs of the selected blade-root bending moment, tower-base bending moment, yaw-bearing moment, and critical fairlead-line tension, respectively. For each matched combination of wind speed, wind direction, turbulent seed, and control strategy, the farm-level DEL is defined as the maximum turbine-level DEL among the four turbines. The relative change is then calculated with respect to the corresponding greedy case. Bars show the mean of the five seed-wise relative changes, and error bars indicate their standard deviation. Positive and negative values denote increased and reduced fatigue loading relative to greedy operation, respectively.

The condition-resolved turbine-level results in Appendix B, Figures B1–B4, provide additional information on the spatial origin of the farm-level DEL changes. They show that several responses are highly localized and may change sign between turbines and operating conditions. The farm-level maximum-DEL metric therefore provides a conservative envelope but does not indicate whether the governing response originates from the upstream or downstream part of the farm. In particular, the large tower-base and fairlead DEL increases are concentrated in specific turbines and wind conditions, whereas the yaw-bearing moment exhibits a more systematic controller-dependent response across the downstream turbines.

3.5 Spectral analysis of power and load fluctuations

Before selecting the load components for the spectral analysis, a DEL-based screening was performed over the complete simulation matrix. For each load component, the relative DEL variation with respect to the matched greedy baseline was evaluated for all wind speeds, wind directions, turbulent seeds, turbines, and control strategies. The load components were then ranked according to two criteria: the mean absolute controller-induced DEL change relative to the matched greedy baseline, and the separation of the mean DEL changes among wake steering, induction, and hybrid control. This screening showed that yaw-bearing DEL was the most sensitive load component, followed by fairlead tension and tower-base moment DEL, whereas blade-root moment DEL exhibited comparatively smaller variations. Accordingly, generator power was retained as the principal performance response, while yaw-bearing moment and fairlead tension were selected as the two load responses for the spectral analysis.

To provide frequency-resolved context for the power-fluctuation and DEL trends, PSD ratios were evaluated for the representative condition $U = 9\ \mathrm{m\,s^{-1}}$ and $\mathrm{WD} = -5^\circ$. This condition was selected because it exhibits pronounced controller-induced changes under substantial wake interaction. For each turbine, control strategy, and turbulent seed, the controlled power-spectral density was normalized by the matched greedy spectrum of the same turbine and seed:

$$R^{(s)}_{\mathrm{PSD}}(f) = \frac{S^{(s)}_{\mathrm{ctrl}}(f)}{S^{(s)}_{\mathrm{greedy}}(f)}, \tag{19}$$

where s denotes the turbulent seed. The seed-level ratios were subsequently averaged over the five seeds:

$$\overline{R}_{\mathrm{PSD}}(f) = \frac{1}{N_s}\sum_{s=1}^{N_s} R^{(s)}_{\mathrm{PSD}}(f), \qquad N_s = 5. \tag{20}$$

Accordingly, the horizontal line at unity denotes an unchanged PSD level at the corresponding frequency relative to greedy operation, whereas values above and below unity indicate spectral amplification and attenuation, respectively. In all three spectral figures, the shaded bands indicate the low-frequency platform-motion, coupled pitch–heave, 1P, wave-excitation, 3P, first tower-mode, first blade-mode, and 9P frequency ranges. The same bands are shown in all turbine panels, with their labels provided only in panel (a) for clarity. The ordinate limits differ among panels to retain the turbine-specific spectral structure. Because the ratio may become large at frequencies where the matched greedy PSD is small, narrow high-amplitude peaks are interpreted as strong relative changes rather than direct measures of absolute spectral energy or fatigue contribution.

Figure 10 shows the turbine-level generator-power PSD ratios relative to the corresponding cases with greedy control. Wake steering produces comparatively small changes in the power-fluctuation spectrum, with the PSD ratio remaining close to unity over most frequency ranges. In contrast, induction and hybrid control produce strong, frequency-selective amplification, particularly in the coupled pitch–heave and 1P ranges and, for some turbines, around 3P and at higher frequencies.

For T1, induction and hybrid control produce the strongest amplification between approximately 0.03 and 0.10 Hz, covering the coupled pitch–heave and 1P ranges, with the largest narrow peak occurring near 1P. T2 exhibits a similarly strong induction-control response below 0.10 Hz, together with a pronounced higher-frequency peak under hybrid control. For T3, the dominant amplification remains concentrated near the 1P range, although additional peaks appear at higher frequencies. In contrast, the T4 response is dominated by induction-control amplification around the 3P range, together with additional peaks in the higher-frequency rotor-harmonic and structural-mode regions. These results show that induction-based control modifies not only the mean turbine power but also its frequency content, with the dominant response shifting along the turbine row.

https://doi.org/10.5194/wes-2026-142
Preprint. Discussion started: 18 August 2026

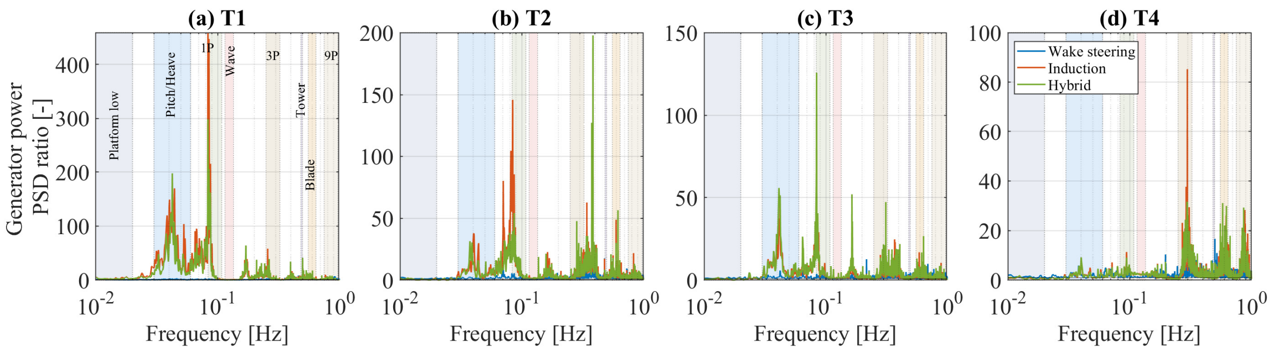

Figure 10. Generator-power spectral response. Turbine-level power-spectral-density ratios of generator power relative to the matched greedy baseline for the representative condition $U = 9\ \mathrm{m\,s^{-1}}$ and $\mathrm{WD} = -5°$. Panels (a)–(d) correspond to turbines T1–T4, respectively. The plotted ratios are averages over five turbulent seeds.

Figure 11 shows the yaw-bearing-moment PSD ratios. This load component was selected because the DEL screening identified the yaw-bearing DEL as the most control-sensitive component. The marked platform-yaw, platform-pitch, wave, 1P, 3P, and tower-mode regions help identify the frequency ranges associated with the yaw-bearing load changes observed in the fatigue analysis. Low-frequency changes are comparatively moderate, whereas the largest ratios occur mainly in the 3P and higher-frequency rotor-harmonic and structural-mode ranges. Wake steering produces a broader moderate amplification over part of the mid-frequency range, while induction and hybrid control generate sharper localized peaks. The strongest high-frequency amplification occurs for T3 and T4, suggesting greater sensitivity of the downstream yaw-bearing response to wake-induced inflow unsteadiness.

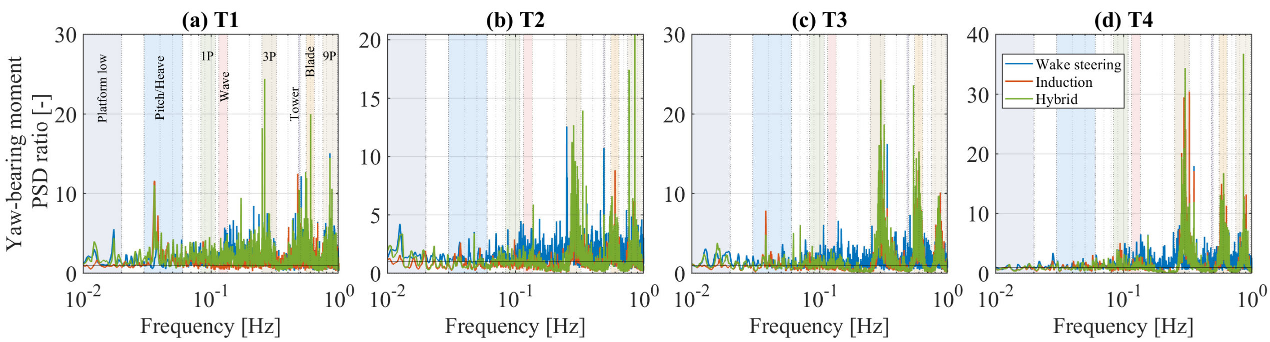

Figure 11. Yaw-bearing spectral response. Turbine-level power-spectral-density (PSD) ratios of the yaw-bearing moment relative to the matched greedy baseline for the representative condition $U = 9\ \mathrm{m\,s^{-1}}$ and $\mathrm{WD} = -5°$. Panels (a)–(d) correspond to turbines T1–T4, respectively.

For each turbine, the fairlead line exhibiting the largest mean absolute controller-induced DEL variation among the three fairlead lines was selected for the PSD analysis. The same fairlead line was used consistently for the matched greedy and controlled cases.

Figure 12 shows that the selected fairlead tension response is mainly affected in the low-frequency platform–mooring and coupled platform-motion ranges. The low-frequency region around $\mathcal{O}(10^{-2})$ Hz is associated with surge/yaw/mooring dy-
585 namics, while the coupled platform-motion band includes pitch- and heave-related response. Additional peaks are visible in the higher-frequency range, especially near the rotor-harmonic and tower-mode regions, but these are interpreted as secondary compared with the low-frequency mooring response.

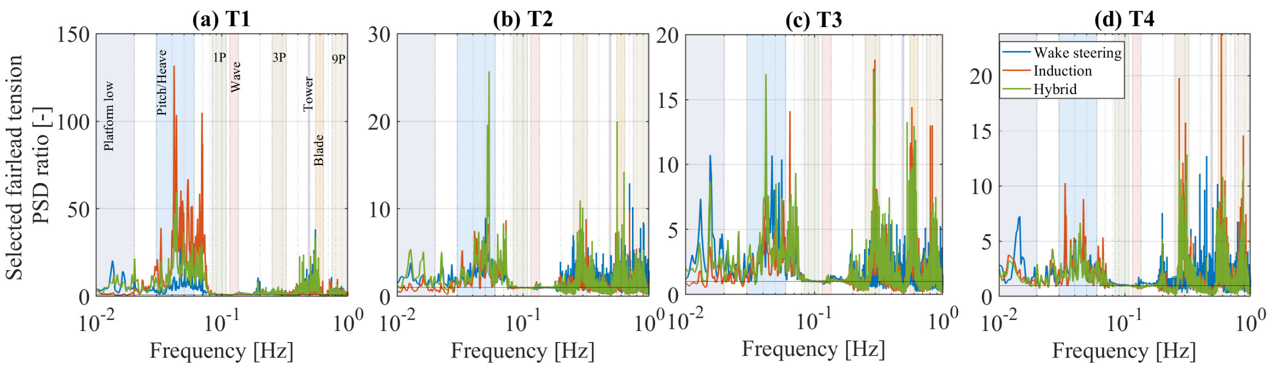

Figure 12. Fairlead-tension spectral response. Turbine-level power-spectral-density (PSD) ratios of the selected fairlead tension relative to the matched greedy baseline for the representative condition $U = 9\,\mathrm{m\,s^{-1}}$ and $\mathrm{WD} = -5°$. Panels (a)–(d) correspond to turbines T1–T4, respectively.

3.6 Power–load trade-off and control strategy ranking

The previous sections showed that the control strategies affect energy production and fatigue loading in different ways. There-
590 fore, the controllers are compared here using a power–load trade-off analysis. For each wind speed, wind direction, control strategy, and turbulent seed, the farm-power gain and farm-level DEL variation were computed relative to the matched case with greedy baseline control. The farm-level DEL was defined conservatively as the maximum DEL among the four turbines for each load component, so that local load increases are not masked by reductions on other turbines.

Figure 13 shows the resulting trade-off maps. The rows separate the three wind speeds, while the columns correspond to the
595 blade-root, tower-base, yaw-bearing moments, and fairlead tension DEL variations. This layout avoids averaging over wind speed and therefore preserves the dependence of the trade-off on operating condition. Points in the lower-right region represent the most favorable trade-off, combining a positive farm-power gain with a reduction in the corresponding farm-level DEL. However, the preferred controller may differ among load components because each panel represents a separate power–load objective.

https://doi.org/10.5194/wes-2026-142
Preprint. Discussion started: 18 August 2026

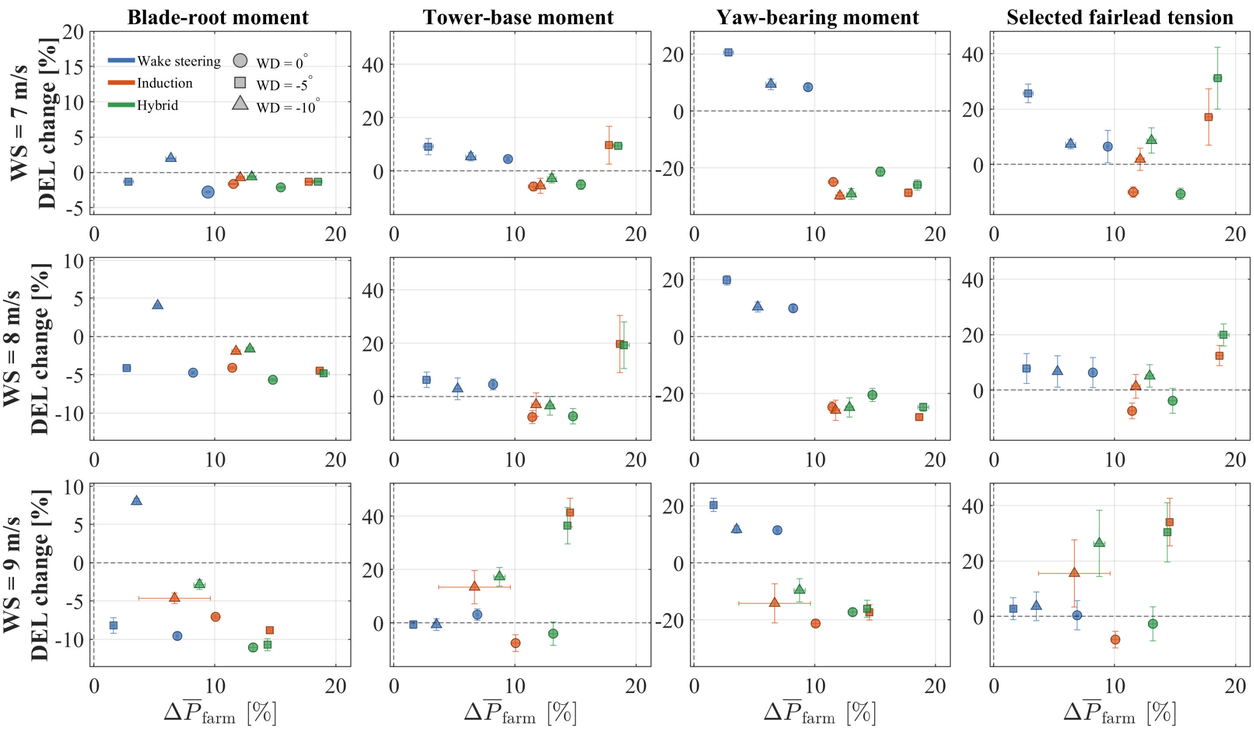

Figure 13. Power–load trade-off of the control strategies. Power–load trade-off of the control strategies relative to the matched greedy baseline. Rows correspond to wind speeds of 7, 8, and 9 m/s, and columns correspond to blade-root, tower-base, yaw-bearing, and fairlead DEL variations. Each marker represents one wind-direction condition averaged over the five turbulent seeds. Marker color indicates the control strategy, marker shape indicates the inflow direction, and horizontal and vertical error bars indicate the standard deviations of the farm-power gain and DEL variation across the five turbulent seeds, respectively.

Figure 13 shows a clear trend in the trade–off by different controllers. Wake steering consistently provides smaller farm-power gains than induction and hybrid control. It also increases the yaw-bearing DEL for all investigated wind speeds and directions. Its effects on the other load components are more condition dependent: blade-root DEL is generally reduced except at WD $= -10°$, while tower-base and selected-fairlead DELs are predominantly increased or remain close to the greedy level. In contrast, induction and hybrid control provide substantially larger farm-power gains and consistently reduce yaw-bearing DEL across all investigated conditions. They also generally reduce blade-root DEL. However, their effects on tower-base and selected-fairlead DELs depend strongly on wind direction, and large load increases occur for some conditions despite the favorable yaw-bearing response.

Blade-root moment DEL changes are comparatively small relative to the other load components. Induction and hybrid control generally reduce it, with the largest reductions occurring at $9\,\mathrm{m\,s^{-1}}$. Wake steering is more direction dependent, producing reductions at WD $= 0°$ and $-5°$, but increases at WD $= -10°$. The tower-base response exhibits a pronounced wind-direction dependence. At WD $= 0°$, induction and hybrid control generally reduce tower-base DEL while maintaining substantial power

https://doi.org/10.5194/wes-2026-142
Preprint. Discussion started: 18 August 2026

gains. At $\mathrm{WD} = -5°$, however, both controllers increase tower-base DEL, and this penalty becomes especially large at $9\ \mathrm{m\,s^{-1}}$. Positive tower-base DEL changes are also observed at $\mathrm{WD} = -10°$ for the $9\ \mathrm{m\,s^{-1}}$ condition.

Overall, no controller provides a uniformly superior power–load trade-off across all load components. Induction and hybrid control dominate wake steering in terms of farm-power gain and yaw-bearing DEL reduction, and they also generally reduce blade-root DEL. Their principal limitation is the direction-dependent increase in tower-base and selected-fairlead DEL, particularly at $\mathrm{WD} = -5°$ and at $9\ \mathrm{m\,s^{-1}}$. The hybrid controller often provides power gains comparable to or slightly greater than induction control and favorable blade-root reductions, but it can incur larger mooring-load penalties. Consequently, the preferred strategy depends on the relative weighting assigned to power production, yaw-bearing fatigue, structural loading, and mooring-system fatigue.

4 Discussion

The present results demonstrate that closed-loop, load-constrained farm-power optimization can increase the power extraction of a floating wind farm, while also showing that the resulting structural and mooring-load responses depend strongly on the selected control strategy and operating condition. In the induction and hybrid controllers, FLORIS maximizes predicted farm power subject to a farm-level rotor-thrust constraint. This constraint limits the aggregate aerodynamic thrust associated with the optimized setpoints, but it does not directly constrain component-level fatigue loads such as blade-root, tower-base, yaw-bearing moments, or fairlead-tension DELs. These quantities are instead evaluated a posteriori from the FAST.Farm simulations.

Induction and hybrid control produce the largest farm-power gains and generally reduce yaw-bearing and blade-root moment DELs, whereas tower-base moment and selected-fairlead responses exhibit operating-condition-dependent penalties. Wake steering provides smaller power gains for several investigated conditions and produces a less favorable yaw-bearing response. Consequently, the principal result is not the identification of a universally superior controller, but the demonstration that different implementations of load-constrained closed-loop control produce distinct power–load balances that vary with wind speed and wind direction.

The turbine-level power and thrust lookup tables used by FLORIS were derived for the considered derating setpoints, and the FLORIS wake model was calibrated against selected FAST.Farm results. FAST.Farm has previously been validated against high-fidelity simulations and full-scale measurements for wake characteristics, turbine power, and structural response, and recent studies have extended this validation to floating-wind-turbine wake behavior. Nevertheless, the specific operating regime considered here—combining pitch-based derating, intentional yaw misalignment, floating-platform motion, and multiple interacting wakes—has not yet been validated to the same extent. The remaining uncertainty therefore concerns the application of the validated engineering model to this particular combined off-design regime, rather than the general validity of FAST.Farm.

Additional uncertainty concerns the FAST.Farm prediction of the wind-farm response under induction and hybrid control. In the present framework, the yaw and blade-pitch-based derating commands computed by FLORIS are applied to the FAST.Farm plant, where OpenFAST resolves the turbine aero-hydro-servo-elastic response and FAST.Farm represents the resulting wake

https://doi.org/10.5194/wes-2026-142
Preprint. Discussion started: 18 August 2026

evolution. The principal uncertainty is therefore not the specific choice of control setpoints, but the magnitude of the downstream wake recovery predicted after the upstream turbines are derated. The large farm-power gains obtained with both induction and hybrid control arise from a substantial reduction in upstream thrust and power followed by a pronounced recovery of the downstream turbines. If FAST.Farm overpredicts the reduction in wake losses under derated operation, similarly large farm-power gains could be obtained for a broad range of induction setpoints even though the corresponding gains would not be realized in a physical wind farm. This uncertainty also affects hybrid operation, for which yaw misalignment and pitch-based derating act simultaneously and may modify wake deflection, velocity recovery, and wake-added turbulence through coupled nonlinear mechanisms. Although FAST.Farm resolves the combined plant response to both commands, the accuracy of its wake prediction for these specific derated and combined yaw–induction operating conditions has not been established to the same extent as for conventional operating cases. Consequently, the absolute power gains predicted for induction and hybrid control should be interpreted cautiously until the corresponding wake recovery is assessed against higher-fidelity simulations, experiments, or field measurements. Recent work on combined yaw and induction control suggests that a dedicated combined formulation may be required instead of assuming that the two effects can be represented through a sequential or approximately superposed treatment (Heck et al., 2025). This aspect should be investigated before drawing quantitative conclusions regarding the absolute performance of the hybrid controller.

This distinction is visible in the tower-base moment and fairlead results. Although induction and hybrid control reduce aggregate rotor thrust relative to their respective reference conditions, some operating conditions exhibit increased tower-base moments or fairlead-tension DELs. These increases arise from the coupled dynamic response of the rotor, tower, floating platform, and mooring system and cannot be inferred solely from the mean farm rotor thrust. The results therefore show that a rotor-thrust constraint can help bound aerodynamic loading during power optimization, but cannot replace an explicit evaluation of structural and mooring loads.

Future work should therefore build on the existing validation of FAST.Farm by targeting the specific non-greedy operating regimes considered here. Derated, yaw-misaligned, and combined yaw–induction cases should be compared with higher-fidelity simulations, wind-tunnel measurements, or field observations in terms of downstream velocity deficit, wake-added turbulence, wake deflection, turbine-power redistribution, and structural and mooring response. The FLORIS calibration could then be extended to include these combined off-design conditions, and yaw and induction setpoints could be optimized simultaneously rather than sequentially. Such validation would reduce uncertainty in the absolute predicted gains while retaining the present comparative conclusions regarding the controller-dependent power–load balances.

Overall, the main contribution of this work is the development of closed-loop wake-steering, induction, and hybrid control strategies within a load-constrained farm-power-optimization framework for a floating wind farm. The results show that closed-loop farm coordination can provide substantial power benefits, but that different implementations produce markedly different structural and mooring-load consequences. In particular, induction and hybrid control improve farm power and generally reduce yaw-bearing and blade-root fatigue over the investigated conditions, while their effects on tower-base and mooring loads depend strongly on wind speed and direction. Controller selection should therefore be based on an operating-condition-dependent power–load assessment rather than on farm-power gain or aggregate rotor thrust alone.

https://doi.org/10.5194/wes-2026-142
Preprint. Discussion started: 18 August 2026

5 Conclusions

This work investigated static, closed-loop wake steering, pitch-based induction control, and hybrid yaw–induction control for a floating wind farm using a coupled FLORIS–ROSCO–FAST.Farm simulation framework. FLORIS was used to optimize the farm-level control setpoints, while FAST.Farm represented the dynamic floating wind-farm plant. For induction and hybrid control, the setpoint optimization maximized predicted farm power subject to a farm-level rotor-thrust constraint. Farm power, rotor thrust, structural fatigue loads, mooring loads, and spectral responses were subsequently evaluated from the FAST.Farm simulations.

The analysis considered a four-turbine array of IEA 15 MW reference wind turbines mounted on UMaine VolturnUS-S platforms under below-rated turbulent inflow. Within the present modeling framework, all three control strategies increased mean farm power relative to the matched greedy baseline. The largest simulated gains were obtained with induction and hybrid control, reaching approximately 18%–19% for the strongest wake-interaction cases. Wake steering produced smaller gains for the same conditions but became more effective when the change in wind direction created a favourable wake-deflection direction.

The turbine-level results showed that the farm-power improvements were obtained by sacrificing power at upstream turbines and recovering a larger amount of power at the downstream turbines. The load response was strongly dependent on the considered component, wind direction, and control strategy. Induction and hybrid control generally reduced blade-root and yaw-bearing DELs, whereas tower-base and fairlead responses were more sensitive to the floating-platform and mooring dynamics. Wake steering was more likely to increase yaw-bearing moment and fairlead tension. The spectral analysis further showed that the effects of farm-level control extend beyond mean power and modify the dynamic response in the platform-motion, rotor-harmonic, and structural-frequency ranges.

Nevertheless, satisfying the aggregate rotor-thrust constraint did not ensure reductions in all component-level fatigue loads. Induction and hybrid control generally reduced blade-root and yaw-bearing DELs, whereas tower-base and fairlead responses were more sensitive to wind direction and to the coupled floating-platform and mooring dynamics. Wake steering was more likely to increase yaw-bearing moment and selected fairlead-tension DELs. These results demonstrate that mean farm rotor thrust is a useful aerodynamic load-related proxy, but it does not fully represent the dynamic structural and mooring-load response of a floating wind farm.

Consequently, no control strategy provided a uniformly superior power–load trade-off across all investigated conditions. Induction and hybrid control were favorable when farm power and yaw-bearing or blade-root fatigue were prioritized, but they could introduce tower-base or mooring-load penalties. Hybrid control often achieved power gains comparable to or greater than induction control, although it also produced some of the largest selected-fairlead DEL increases. The preferred closed-loop implementation therefore depends on the operating condition and on the relative importance assigned to power production, structural fatigue, and mooring-system loading.

Future work should extend the validation of the modeling framework to pitch-derated, yaw-misaligned, and combined yaw–induction operating conditions using higher-fidelity simulations, wind-tunnel experiments, or field measurements. Particular attention should be given to downstream velocity recovery, wake-added turbulence, wake deflection, turbine-power redistribution, and structural and mooring response. The FLORIS calibration could subsequently be extended to include these non-greedy conditions, and fully coupled yaw–induction optimization formulations should be assessed.

The load-constrained optimization should also be extended beyond the present farm-level rotor-thrust proxy. In this work, rotor thrust is used as an aerodynamic load-related constraint because it can be evaluated efficiently in FLORIS during online optimization. However, the FAST.Farm results show that component-level fatigue responses, especially tower-base moments and fairlead-line tensions, are governed by coupled aerodynamic, structural, platform, and mooring dynamics that are not captured by mean rotor thrust alone. Future work should therefore develop reduced-order or surrogate load models capable of predicting blade-root, tower-base, yaw-bearing, and mooring fatigue indicators from the farm operating state and control setpoints. Such models could then be incorporated directly into the supervisory optimization to enable explicit power–load or fatigue-constrained control, rather than using aggregate rotor thrust as the only load-related proxy.

Further investigations should consider broader wind-speed, wind-direction, turbulence, and wave conditions, larger wind-farm layouts, and alternative floating-platform and mooring configurations. Such studies are needed to determine whether the observed controller rankings remain valid beyond the present four-turbine configuration.

Overall, the results demonstrate the potential of static closed-loop control to increase floating wind-farm power while limiting aggregate aerodynamic rotor thrust. At the same time, they show that a farm-level thrust constraint alone is insufficient to control all structural and mooring-load consequences. The coupled framework presented here provides a means of performing load-constrained farm-power optimization, evaluating the resulting dynamic power–load trade-offs, identifying conditions in which power gains are accompanied by structural or mooring penalties, and supporting the development of more comprehensive load-aware control strategies for future floating wind farms.

Acknowledgements

F.B. and M.E. acknowledge financial support for their doctoral scholarships within the framework of the Italian National Recovery and Resilience Plan (PNRR), with co-funding from Eni S.p.A. The authors acknowledge CFDHub@Polimi, the interdepartmental high-performance computing infrastructure of Politecnico di Milano, for providing the computational resources used in this study. The authors also acknowledge the National Laboratory of the Rockies, formerly the National Renewable Energy Laboratory, and the development teams of OpenFAST/FAST.Farm, FLORIS, and ROSCO for developing, maintaining, documenting, and openly releasing the software tools used in this work, including the ROSCO ZeroMQ wind-farm-control interface. During the preparation of this manuscript, the authors used AI for language editing and proofreading. The authors reviewed and edited all outputs and take full responsibility for the content of the manuscript.

Code and data availability. The controller scripts, calibrated FLORIS model files, FAST.Farm/OpenFAST input templates, wind-speed observation routines, post-processing scripts, processed datasets, figure data, and supporting raw FAST.Farm output files used in this study

https://doi.org/10.5194/wes-2026-142
Preprint. Discussion started: 18 August 2026

are publicly available on Zenodo at https://doi.org/10.5281/zenodo.21382660. The archive includes the files needed to reproduce the post-processing and figures presented in the paper.

Appendix A: Fatigue-load calculation

Fatigue loading is assessed through short-term damage-equivalent loads (DELs). A DEL represents the constant-amplitude load, at a prescribed equivalent frequency, that produces the same fatigue damage as the original variable-amplitude load time series. Rainflow counting is used to decompose each load signal into individual cycles characterized by a cycle mean and a cycle range.

The fatigue post-processing is carried out using MLife (Hayman, 2012; Hayman and Buhl Jr., 2012). MLife supports short-term DEL calculations based on uncorrected rainflow ranges or Goodman-corrected ranges about a specified fixed mean. In the present work, Goodman correction is applied and the reported short-term DELs correspond to the fixed-mean formulation. The fixed mean is defined in MLife through `TypeLMF = AM`, meaning that, for each fatigue component, the fixed mean is computed from the aggregate mean across the input files. Accordingly, the reported DELs retain the influence of nonzero cycle means through the Goodman correction and are expressed with respect to a fixed-mean reference representative of the analyzed dataset.

The reported DELs are one-sided amplitudes at an equivalent frequency of 1 Hz.

Following the Palmgren–Miner linear damage accumulation hypothesis, the cumulative fatigue damage is given by Eq. (A1):

$$D = \sum_i \frac{n_i}{N_i}, \tag{A1}$$

where n_i is the number of occurrences of cycle i and N_i is the corresponding number of cycles to failure. Using a single-slope S–N representation, the cycles to failure are given by Eq. (A2)

$$N_i = \left(\frac{L^{\mathrm{ult}} - |L^{MF}|}{L_i^{RF}/2} \right)^m, \tag{A2}$$

where L^{ult} is the ultimate load of the considered component, L^{MF} is the fixed mean load, L_i^{RF} is the Goodman-corrected cycle range, and m is the Wöhler exponent. In this work, $m = 4$ is used for steel components of the tower, $m = 3$ for the mooring-line tensions, and $m = 10$ for blade composite components. Because the original rainflow cycles occur at different mean loads, the cycle ranges are corrected using the Goodman relation in Eq. (A3),

$$L_i^{RF} = L_i^R \left(\frac{L^{\mathrm{ult}} - |L^{MF}|}{L^{\mathrm{ult}} - |L_i^M|} \right), \tag{A3}$$

where L_i^R is the raw rainflow range and L_i^M is the mean load of cycle i. The Goodman correction is introduced to account for the influence of the cycle mean on fatigue damage. For each time series, the short-term fixed-mean DEL is then computed as in Eq. (A4):

$$\mathrm{DEL}^{ST,F} = \left(\frac{\sum_i n_i \left(L_i^{RF}\right)^m}{n^{eq}} \right)^{1/m}, \tag{A4}$$

775 where n_{eq} denotes the equivalent number of load cycles and is calculated using Eq. (A5).

$$n^{eq} = f^{eq} T, \tag{A5}$$

where $f^{eq} = 1$ Hz is the equivalent DEL frequency and T is the duration of the analyzed time series. To account for load directionality, the DELs are computed along multiple directions θ within the blade-root, tower-base, and yaw-bearing cross-sections as in Eq. (A6)

780 $$M(t,\theta) = M_x(t)\cos(\theta) + M_y(t)\sin(\theta), \tag{A6}$$

where M_x and M_y are the moments along two orthogonal directions. The load-rose directions are generated in MLife from the specified number of sectors, and the maximum DEL over the considered sectors is reported for each grouped component. For blade-root and tower-base bending moments, the ultimate load used in the Goodman correction is estimated following the approach of Carmo et al. (2024), as given in Eq. (A7):

785 $$L_{\mathrm{ult}} = \sigma_{\mathrm{ult}} \frac{I}{R}, \tag{A7}$$

where σ_{ult} is the ultimate stress, I is the second moment of area, and R is the outer radius of the cross-section. In this work, $\sigma_{\mathrm{ult}} = 1000\ \mathrm{MPa}$ is used for the composite blade root and $\sigma_{\mathrm{ult}} = 300\ \mathrm{MPa}$ for the steel tower, consistent with the assumptions considered in Carmo et al. (2024). The blade-root section is approximated as a circular tubular section with root diameter $D = 5.20$ m and wall thickness $t = 0.1R$, while the tower-base properties are taken from the VolturnUS-S floating support 790 documentation. For the mooring-line tension component, the ultimate load is taken directly as the documented line breaking strength (Allen et al., 2020).

Because a reliable public ultimate-load reference for the IEA 15-MW yaw-bearing moments was not available, the yaw-bearing components were assigned a sufficiently large assumed L_{ult} in the MLife setup. For the yaw-bearing moments, the assumed reference value used in the MLife setup was $L_{\mathrm{ult}} = 1906.452\ \mathrm{MN\,m}$.

795 Table A2 summarizes the load variables used in the fatigue post-processing. For the tower base and blade root, orthogonal bending components are combined into load roses using the standard side-to-side/fore-aft and edgewise/flapwise moment pairs, respectively. For the yaw bearing, the load rose is constructed from the two orthogonal bending components in the nonrotating frame, namely the roll and pitch moments at the tower-top/yaw-bearing interface. The yaw-bearing torsional moment is not combined in the same load rose because it represents a yaw-axis moment rather than an orthogonal bending component.

https://doi.org/10.5194/wes-2026-142
Preprint. Discussion started: 18 August 2026

eawe european academy of wind energy
Open Access WIND ENERGY SCIENCE DISCUSSIONS

800 ## Appendix B: Condition-resolved turbine-level fatigue-load response

Figures B1–B4 present the condition-resolved turbine-level fatigue response for the selected load channels. For each turbine, control strategy, wind speed, wind direction, and turbulent seed, the relative DEL change is calculated as

$$\Delta\mathrm{DEL} = 100\frac{\mathrm{DEL}_{\mathrm{control}} - \mathrm{DEL}_{\mathrm{greedy}}}{|\mathrm{DEL}_{\mathrm{greedy}}|}. \tag{B1}$$

Each heatmap cell reports the arithmetic mean of the relative DEL changes over the five matched turbulent seeds. Wind
805 speed and wind direction are not averaged. Positive values indicate increased fatigue loading relative to the matched greedy case, whereas negative values indicate a reduction. The greedy strategy is not shown as a separate row because it defines the zero-reference condition.

Figure B1 shows that the blade-root bending-moment response is generally moderate and strongly turbine-dependent. Induction and hybrid control reduce the DEL at T1 for nearly all investigated conditions, with the largest reductions occurring
810 at $9\ \mathrm{m/s}$. However, small increases can occur at downstream turbines, particularly at the higher wind speeds. Wake steering produces reductions at $WD = 0°$ and $WD = -5°$, but increases the blade-root DEL at several downstream turbines for $WD = -10°$. These results explain why the farm-level blade-root response changes with inflow direction despite the relatively small turbine-level changes in most cases.

Table A1. Parameters and equations used to compute ultimate loads for the main components considered in the Goodman-corrected DEL analysis (IEA 15-MW / VolturnUS-S).

Parameter	Blade root	Tower base	Mooring line
Wöhler exponent m	10	4	3
Reference diameter D [m]	5.20	10.00	–
Thickness t [mm]	260	82.954	–
Ultimate stress σ_{ult} [MPa]	1000	300	–
L_{ult} definition	$\sigma_{\mathrm{ult}} I/R$	$\sigma_{\mathrm{ult}} I/R$	Breaking strength
L_{ult} [MN m or MN]	4747	1906	22.286

https://doi.org/10.5194/wes-2026-142
Preprint. Discussion started: 18 August 2026

Open Access
WIND ENERGY SCIENCE DISCUSSIONS

Table A2. Paired load variables used for DEL post-processing.

Component	Variable pair	Physical interpretation
Tower base	`TwrBsMxt`, `TwrBsMyt`	Side-to-side and fore-aft bending moments
Blade root	`RootMxb1`, `RootMyb1`	Edgewise and flapwise bending moments
Yaw bearing	`YawBrMxp`, `YawBrMyp`	Roll and pitch bending moments in the nonrotating frame

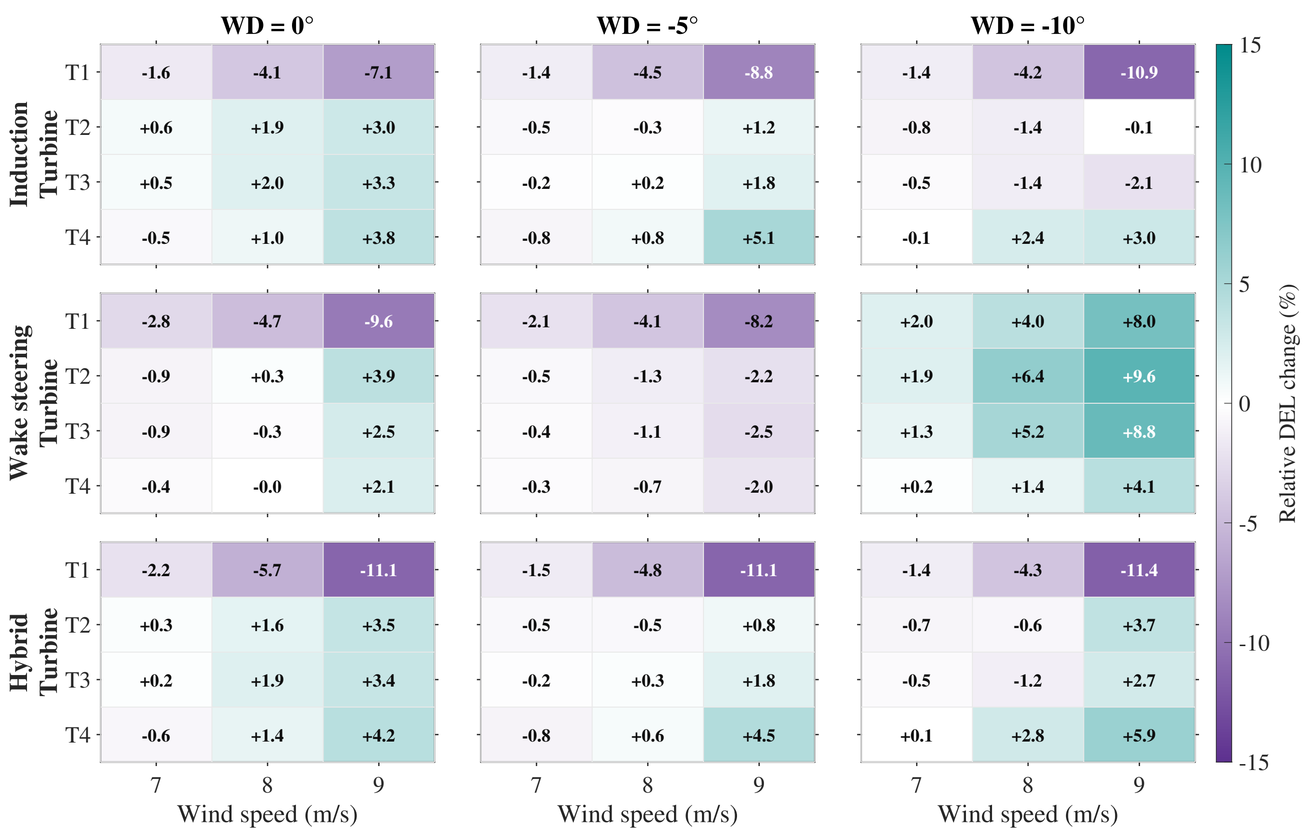

Figure B1. Turbine-level blade-root DEL response. Condition-resolved turbine-level relative change in the blade-root moment DEL. Rows of panels correspond to induction control, wake steering, and hybrid control, while columns correspond to $WD = 0°$, $-5°$, and $-10°$. Within each panel, rows represent turbines T1–T4 and columns represent wind speeds of 7, 8, and 9 $\mathrm{m/s}$. Each cell shows the mean relative DEL change over the five matched turbulent seeds. Positive and negative values indicate increases and reductions relative to greedy operation, respectively.

Figure B2 demonstrates that the tower-base bending-moment response is highly localized. Under induction and hybrid control, the largest increases occur at T1 for $WD = -5°$, especially at 9 $\mathrm{m/s}$. Additional increases appear at downstream turbines for $WD = -10°$ and 9 $\mathrm{m/s}$, while reductions are observed for many $WD = 0°$ cases. Wake steering produces a

https://doi.org/10.5194/wes-2026-142
Preprint. Discussion started: 18 August 2026

different spatial distribution, generally increasing the tower-base DEL at T2–T4 while maintaining or reducing it at T1. Thus, the farm-level maximum is governed by different turbines depending on the control strategy and operating condition.

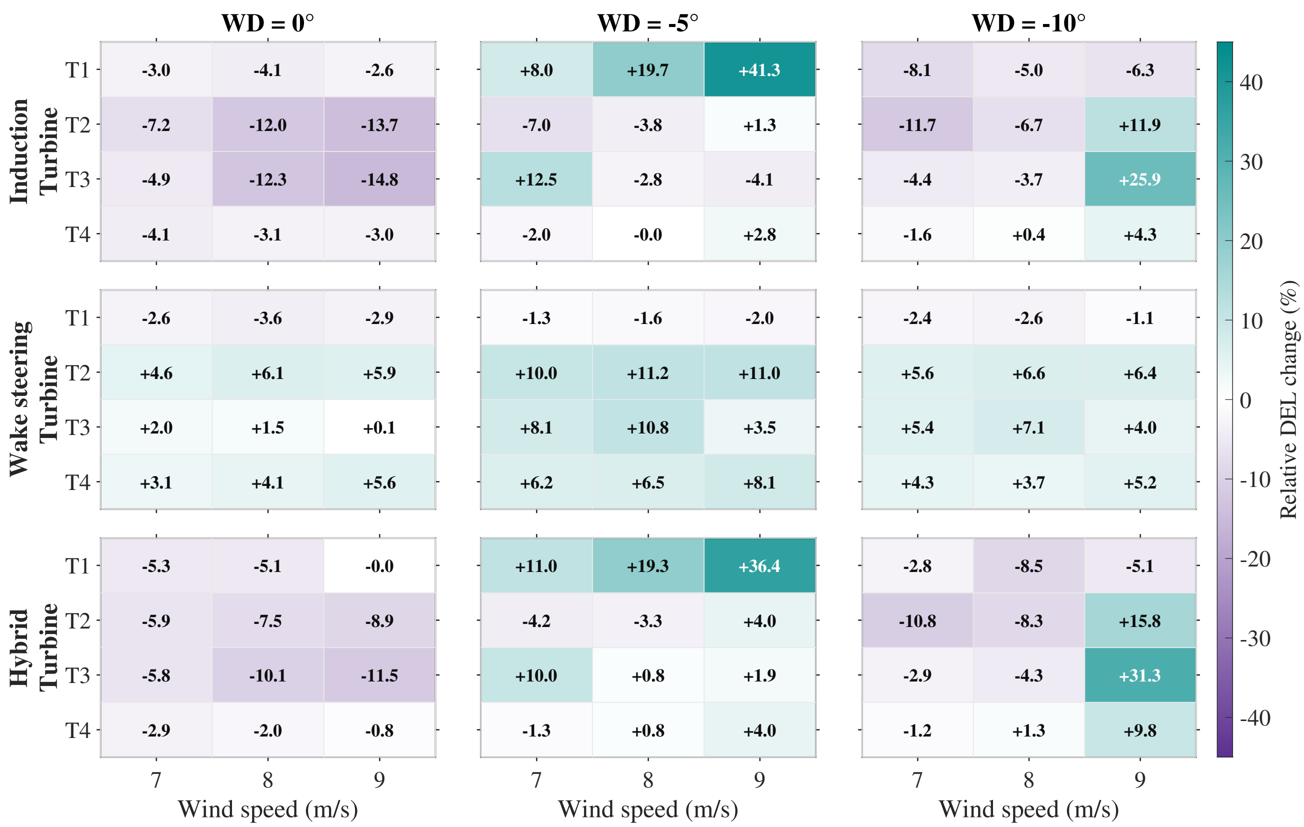

Figure B2. Turbine-level tower-base DEL response. Condition-resolved turbine-level relative change in the tower-base bending-moment DEL. Rows of panels correspond to induction control, wake steering, and hybrid control, while columns correspond to $WD = 0°$, $-5°$, and $-10°$. Within each panel, rows represent turbines T1–T4 and columns represent wind speeds of 7, 8, and 9 $\mathrm{m/s}$. Each cell shows the mean relative DEL change over the five matched turbulent seeds. Positive and negative values indicate increases and reductions relative to greedy operation, respectively.

Figure B3 shows the clearest controller-dependent turbine-level trend. Induction and hybrid control substantially reduce the selected yaw-bearing moment DEL at T2–T4 for most conditions, while their changes at T1 remain comparatively small. Wake steering instead increases the yaw-bearing moment DEL at the downstream turbines, with the largest increases occurring at $WD = -5°$. This spatially consistent contrast explains the systematic farm-level separation between wake steering and the pitch-based control strategies.

https://doi.org/10.5194/wes-2026-142
Preprint. Discussion started: 18 August 2026

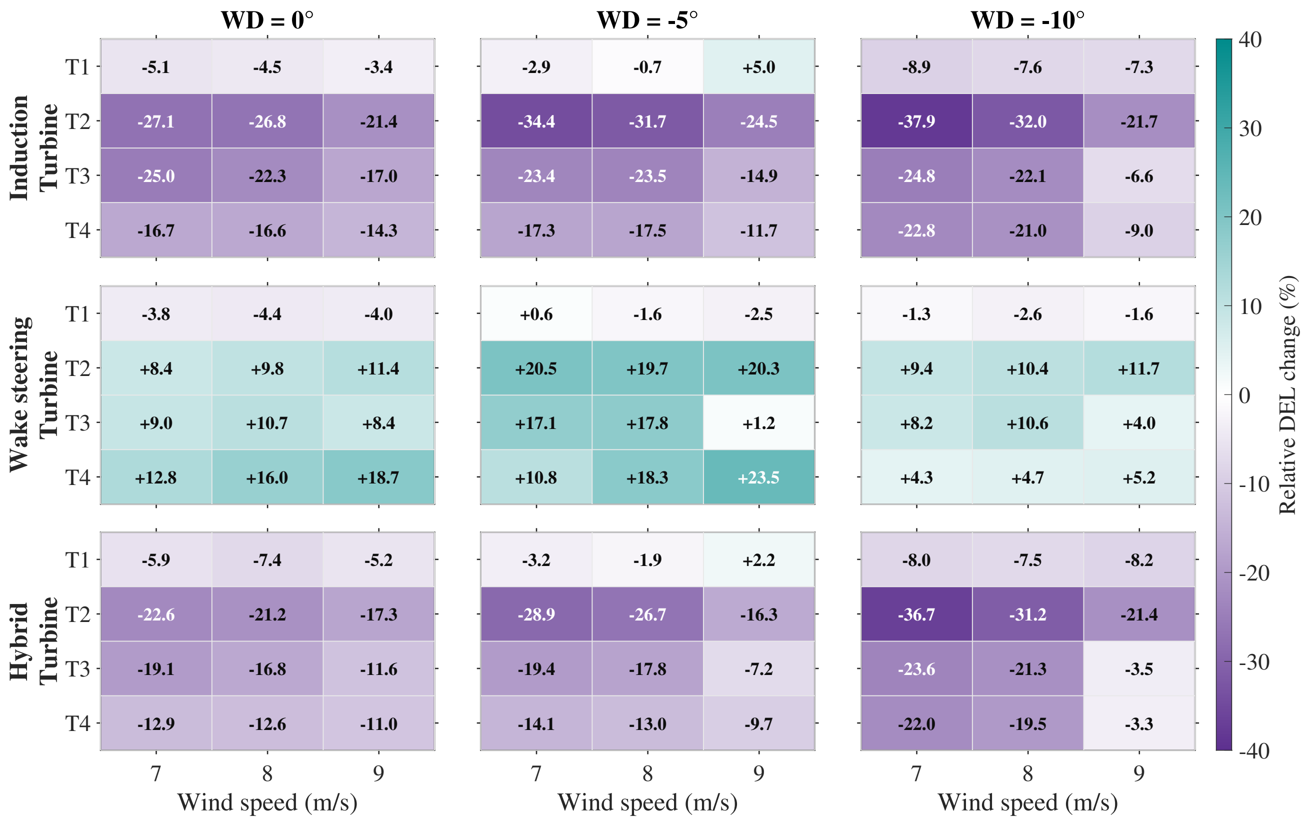

Figure B3. Turbine-level yaw-bearing DEL response. Condition-resolved turbine-level relative change in the yaw-bearing moment DEL. Rows of panels correspond to induction control, wake steering, and hybrid control, while columns correspond to $WD = 0°$, $-5°$, and $-10°$. Within each panel, rows represent turbines T1–T4 and columns represent wind speeds of 7, 8, and 9 $\mathrm{m/s}$. Each cell shows the mean relative DEL change over the five matched turbulent seeds. Positive and negative values indicate increases and reductions relative to greedy operation, respectively.

Figure B4 confirms that the critical fairlead-line tension response is strongly condition- and turbine-dependent. Induction and hybrid control generally reduce the fairlead DEL at $WD = 0°$, but can produce large increases at T1 for $WD = -5°$ and at downstream turbines for $WD = -10°$ and 9 $\mathrm{m/s}$. Wake steering produces a different distribution, with increased fairlead DEL primarily at T2–T4 for several conditions. Because the governing turbine changes across the operating matrix, the fairlead response should not be represented by a single turbine-level average over all wind conditions.

https://doi.org/10.5194/wes-2026-142
Preprint. Discussion started: 18 August 2026

WIND ENERGY SCIENCE DISCUSSIONS

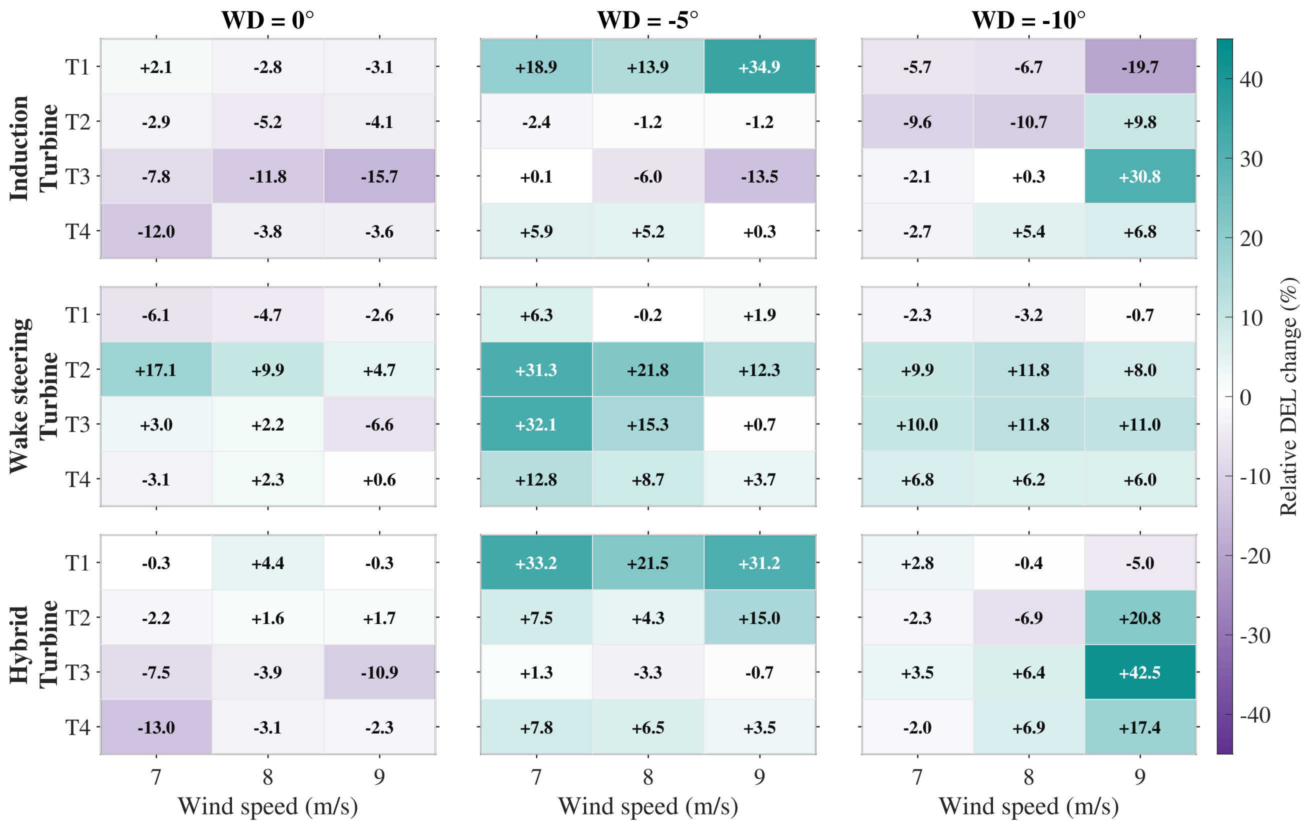

Figure B4. Turbine-level fairlead-tension DEL response. Condition-resolved turbine-level relative change in the critical fairlead-line tension DEL. Rows of panels correspond to induction control, wake steering, and hybrid control, while columns correspond to $WD = 0°$, $-5°$, and $-10°$. Within each panel, rows represent turbines T1–T4 and columns represent wind speeds of 7, 8, and $9\ \mathrm{m/s}$. For each turbine, the selected fairlead line is the line exhibiting the largest mean absolute controller-induced DEL variation among the three fairlead lines, and the same line is used consistently for the matched greedy and controlled cases. Each cell shows the mean relative DEL change over the five matched turbulent seeds. Positive and negative values indicate increases and reductions relative to greedy operation, respectively.

Author contributions. ME and FB contributed equally to this work. ME developed the numerical framework, performed the simulations, conducted the post-processing, and prepared the original manuscript. FB contributed to the methodology, software implementation, validation, interpretation of the results, and review and editing of the manuscript. AF contributed to the methodology, validation, supervision, and review and editing. SM and MB contributed to the conceptualization, supervision, project administration, and review and editing. All authors discussed the results and approved the final manuscript.

Competing interests. The authors declare that they have no conflict of interest.

https://doi.org/10.5194/wes-2026-142
Preprint. Discussion started: 18 August 2026

References

Abbas, N. J., Zalkind, D. S., Pao, L., and Wright, A.: A reference open-source controller for fixed and floating offshore wind turbines, Wind Energy Science, 7, 53–73, 2022.

Ali, A., Shi, W., Wang, S., Zhai, H., Haider, R., Leng, S., Li, X., and Han, X.: Dynamic analysis of a TetraSpar floating offshore wind turbine with different tendons failure scenario, Ocean Engineering, 323, 120 607, 2025.

Allen, C., Viscelli, A., Dagher, H., Goupee, A., Gaertner, E., Abbas, N., Hall, M., and Barter, G.: Definition of the UMaine VolturnUS-S reference platform developed for the IEA wind 15-megawatt offshore reference wind turbine, Tech. rep., National Renewable Energy Laboratory (NREL), Golden, CO, United States, 2020.

Annoni, J., Fleming, P., Scholbrock, A., Roadman, J., Dana, S., Adcock, C., Porte-Agel, F., Raach, S., Haizmann, F., and Schlipf, D.: Analysis of control-oriented wake modeling tools using lidar field results, Wind Energy Science, 3, 819–831, https://doi.org/10.5194/wes-3-819-2018, 2018.

Baricchio, M., van der Hoek, D., Dammann, T., Gebraad, P. M. O., Iori, J., and van Wingerden, J.-W.: Combining wake steering and active wake mixing on a large-scale wind farm, Wind Energy Science Discussions, 2025, 1–36, https://doi.org/10.5194/wes-2025-265, 2025.

Bastankhah, M. and Porté-Agel, F.: Experimental and theoretical study of wind turbine wakes in yawed conditions, Journal of Fluid Mechanics, 806, 506–541, https://doi.org/10.1017/jfm.2016.595, 2016.

Becker, M., van den Broek, M. J., Allaerts, D., and van Wingerden, J.-W.: Closed-Loop Model-Predictive Wind Farm Flow Control Under Time-Varying Inflow Using FLORIDyn, Wind Energy, 28, e70 044, 2025.

Bellini, F., Ebrahimi, M., Giuseppe, P. D., Fontanella, A., Muggiasca, S., and Belloli, M.: Closed-loop Wind farm control for floating turbines via online yaw and induction setpoint optimization, Journal of Physics: Conference Series, 3224, 032 081, https://doi.org/10.1088/1742-6596/3224/3/032081, 2026.

Boersma, S., Doekemeijer, B. M., Gebraad, P. M., Fleming, P. A., Annoni, J., Scholbrock, A. K., Frederik, J. A., and van Wingerden, J.-W.: A tutorial on control-oriented modeling and control of wind farms, in: 2017 American control conference (ACC), pp. 1–18, IEEE, 2017.

Bossanyi, E. and Ruisi, R.: Axial induction controller field test at Sedini wind farm, Wind Energy Science, 6, 389–408, 2021.

Branlard, E., Martínez-Tossas, L. A., and Jonkman, J.: A time-varying formulation of the curled wake model within the FAST. Farm framework, Wind Energy, 26, 44–63, 2023.

Branlard, E., Jonkman, J., Platt, A., Thedin, R., Martínez-Tossas, L. A., and Kretschmer, M.: Development and Verification of an Improved Wake-Added Turbulence Model in FAST.Farm, Journal of Physics: Conference Series, 2767, 092 036, https://doi.org/10.1088/1742-6596/2767/9/092036, 2024.

Campagnolo, F., Petrović, V., Bottasso, C. L., and Croce, A.: Wind tunnel testing of wake control strategies, in: 2016 American Control Conference (ACC), pp. 513–518, IEEE, 2016.

Carmo, L., Jonkman, J., and Thedin, R.: Investigating the interactions between wakes and floating wind turbines using FAST. Farm, Wind Energy Science, 9, 1827–1847, 2024.

Chanprasert, W., Sharma, R., Cater, J., and Norris, S.: Large Eddy Simulation of wind turbine fatigue loading and yaw dynamics induced by wake turbulence, Renewable Energy, 190, 208–222, 2022.

Doekemeijer, B. M. and van Wingerden, J.-W.: Observability of the ambient conditions in model-based estimation for wind farm control: A focus on static models, Wind Energy, https://doi.org/10.1002/we.2495, 2020.

https://doi.org/10.5194/wes-2026-142
Preprint. Discussion started: 18 August 2026

Doekemeijer, B. M., Van Der Hoek, D., and Van Wingerden, J.-W.: Closed-loop model-based wind farm control using FLORIS under time-varying inflow conditions, Renewable Energy, 156, 719–730, 2020.

Doekemeijer, B. M., Kern, S., Maturu, S., Kanev, S., Salbert, B., Schreiber, J., Campagnolo, F., Bottasso, C. L., Schuler, S., Wilts, F., et al.: Field experiment for open-loop yaw-based wake steering at a commercial onshore wind farm in Italy, Wind Energy Science, 6, 159–176, 2021.

Fleming, P., Annoni, J., Shah, J. J., Wang, L., Ananthan, S., Zhang, Z., Hutchings, K., Wang, P., Chen, W., and Chen, L.: Field test of wake steering at an offshore wind farm, Wind Energy Science, 2, 229–239, 2017.

Fleming, P., King, J., Dykes, K., Simley, E., Roadman, J., Scholbrock, A., Murphy, P., Lundquist, J. K., Moriarty, P., Fleming, K., et al.: Initial results from a field campaign of wake steering applied at a commercial wind farm–Part 1, Wind Energy Science, 4, 273–285, 2019.

Fleming, P., King, J., Bay, C. J., Simley, E., Mudafort, R., Hamilton, N., Farrell, A., and Martinez-Tossas, L.: Overview of FLORIS updates, in: Journal of Physics: Conference Series, vol. 1618, p. 022028, IOP Publishing, 2020.

Fleming, P., Annoni, J., and Mudafort, R.: FLORIS v3. 5 Wake Modeling and Wind Farm Controls Software [SWR-17-43 and SWR-14-20], Tech. rep., National Renewable Energy Laboratory (NREL), Golden, CO (United States), 2023.

Fleming, P. A., Stanley, A. P., Bay, C. J., King, J., Simley, E., Doekemeijer, B. M., and Mudafort, R.: Serial-refine method for fast wake-steering yaw optimization, in: Journal of Physics: Conference Series, vol. 2265, p. 032109, IOP Publishing, 2022.

Fontanella, A., Colpani, G., De Pascali, M., Muggiasca, S., and Belloli, M.: Assessing the impact of waves and platform dynamics on floating wind turbine energy production, Wind Energy Science Discussions, 2023, 1–33, 2023.

Fontanella, A., Youssef Mahfouz, M., De Pascali, M., Wen Cheng, P., and Belloli, M.: Wind tunnel evaluation of aerodynamic loads in FAST. Farm under controlled wake conditions, Wind Energy, 28, e70 026, 2025.

Gaertner, E., Rinker, J., Sethuraman, L., Zahle, F., Anderson, B., Barter, G. E., Abbas, N. J., Meng, F., Bortolotti, P., Skrzypinski, W., et al.: IEA wind TCP task 37: definition of the IEA 15-megawatt offshore reference wind turbine, Tech. rep., National Renewable Energy Lab.(NREL), Golden, CO (United States), 2020.

Hayman, G. J.: MLife Theory Manual for Version 1.00, Tech. rep., National Renewable Energy Laboratory, Golden, CO, 2012.

Hayman, G. J. and Buhl Jr., M. L.: MLife User's Guide for Version 1.00, Tech. rep., National Renewable Energy Laboratory, Golden, CO, 2012.

Heck, K. S., Liew, J., Upfal, I. M., and Howland, M. F.: Joint Yaw-Induction Control Optimization for Wind Farms, Wind Energy Science Discussions, 2025, 1–40, 2025.

Houck, D. and Cowen, E. A.: Power and flow analysis of axial induction control in an array of model-scale wind turbines, Energies, 15, 5347, 2022.

Howland, M. F., Lele, S. K., and Dabiri, J. O.: Wind farm power optimization through wake steering, Proceedings of the National Academy of Sciences, 116, 14 495–14 500, 2019.

Jeans, G.: Converging profile relationships for offshore wind speed and turbulence intensity, Wind Energy Science Discussions, 2023, 1–40, 2023.

Ji, R., Li, X., Ye, Y., Zhu, R., Sun, K., Wu, M., Huang, F., and Reabroy, R.: Hydrodynamic characteristics of offshore wind turbine pile foundations under combined focusing wave-current conditions, Journal of Marine Science and Engineering, 12, 2068, 2024.

Johlas, H. M., Martínez-Tossas, L. A., Schmidt, D. P., Lackner, M. A., and Churchfield, M. J.: Large eddy simulations of floating offshore wind turbine wakes with coupled platform motion, in: Journal of Physics: Conference Series, vol. 1256, p. 012018, IOP Publishing, 2019.

Jonkman, B. et al.: Turbsim user's guide v2. 00.00, Natl. Renew. Energy Lab, 2014.

https://doi.org/10.5194/wes-2026-142
Preprint. Discussion started: 18 August 2026

Jonkman, J., Doubrawa, P., Hamilton, N., Annoni, J., and Fleming, P.: Validation of FAST. Farm against large-eddy simulations, in: Journal of Physics: Conference Series, vol. 1037, p. 062005, IOP Publishing, 2018.

Jonkman, J. M. and Shaler, K.: Fast. farm user's guide and theory manual, National Renewable Energy Laboratory Golden, CO, USA, 2021.

King, J., Fleming, P., King, R., Martínez-Tossas, L. A., Bay, C. J., Mudafort, R., and Simley, E.: Control-oriented model for secondary effects of wake steering, Wind Energy Science, 6, 701–714, 2021.

Lozon, E., Hall, M., and Mahfouz, M. Y.: Coupled modeling of wake steering and platform offsets for floating wind arrays, in: Journal of Physics: Conference Series, vol. 2767, p. 062035, IOP Publishing, 2024.

Martínez-Tossas, L. A., King, J., Quon, E., Bay, C. J., Mudafort, R., Hamilton, N., Howland, M. F., and Fleming, P. A.: The curled wake model: a three-dimensional and extremely fast steady-state wake solver for wind plant flows, Wind Energy Science, 6, 555–570, 2021.

Meyers, J., Bottasso, C., Dykes, K., Fleming, P., Gebraad, P., Giebel, G., Göçmen, T., and Van Wingerden, J.-W.: Wind farm flow control: prospects and challenges, Wind Energy Science Discussions, 2022, 1–56, 2022.

Nash, R., Nouri, R., and Vasel-Be-Hagh, A.: Wind turbine wake control strategies: A review and concept proposal, Energy Conversion and Management, 245, 114 581, https://doi.org/https://doi.org/10.1016/j.enconman.2021.114581, 2021.

Niayifar, A. and Porté-Agel, F.: Analytical Modeling of Wind Farms: A New Approach for Power Prediction, Energies, 9, 741, https://api.semanticscholar.org/CorpusID:10960022, 2016.

NREL ROSCO Developers: ROSCO Documentation: Example 17c_zeromq_fastfarm, https://rosco.readthedocs.io/en/latest/source/examples.html, accessed: 2026-06-17, 2026.

OpenFAST Development Team: OpenFAST Documentation: InflowWind User's Guide and Theory Manual, National Renewable Energy Laboratory / National Laboratory of the Rockies, https://openfast.readthedocs.io/en/main/source/user/inflowwind/index.html, accessed: 2026-06-17, 2026.

Rivera-Arreba, I., Li, Z., Yang, X., and Bachynski-Polić, E. E.: Comparison of the dynamic wake meandering model against large eddy simulation for horizontal and vertical steering of wind turbine wakes, Renewable Energy, 221, 119 807, 2024.

Shaler, K., Debnath, M., and Jonkman, J.: Validation of FAST. farm against full-scale turbine SCADA data for a small wind farm, in: Journal of Physics: Conference Series, vol. 1618, p. 062061, IOP Publishing, 2020.

Sharma, S. and Nava, V.: Condition monitoring of mooring systems for Floating Offshore Wind Turbines using Convolutional Neural Network framework coupled with Autoregressive coefficients, Ocean Engineering, 302, 117 650, 2024.

Simley, E., Fleming, P., Girard, N., Alloin, L., Godefroy, E., and Duc, T.: Results from a wake-steering experiment at a commercial wind plant: investigating the wind speed dependence of wake-steering performance, Wind Energy Science, 6, 1427–1453, 2021.

Thedin, R., Kreeft, J., Barter, G., Jonkman, J., and Shaler, K.: Impact of wake steering on loads of downstream wind turbines at an above-rated condition, in: Journal of Physics: Conference Series, vol. 2767, p. 032020, IOP Publishing, 2024.

Türk, M. and Emeis, S.: The dependence of offshore turbulence intensity on wind speed, Journal of Wind Engineering and Industrial Aerodynamics, 98, 466–471, 2010.

van Binsbergen, D., Daems, P.-J., Verstraeten, T., Nejad, A. R., and Helsen, J.: Hyperparameter tuning framework for calibrating analytical wake models using SCADA data of an offshore wind farm, Wind Energy Science, 9, 1507–1526, 2024.